Pickup Ions at 1 AU

Master Thesis

Institute for Experimental and Applied Physics
Christian-Albrechts-University of Kiel

Andreas Taut

Contents

Abstract

In this Master thesis heavy pickup ions measured with the Charge Time-of-Flight (CTOF) sensor of the Charge, ELement and Isotope Analysis System (CELIAS) onboard the SOlar and Heliospheric Observatory (SOHO) spacecraft at 1 Astronomical Unit (AU) are investigated. Pickup ions (PUI) are former neutral atoms that are ionized in the heliosphere and can be distinguished from solar wind ions by their low charge state and distinct velocity distribution. The neutral atoms can either originate from the interstellar medium (interstellar PUI) or an inner source in the inner heliosphere (inner-source PUI) that is presently not well understood.

CTOF is a time-of-flight spectrometer that can determine an ion's mass, mass-per-charge and energy by the combined measurement of energy-per-charge, time-of-flight and residual energy. Because of CTOF's large geometric factor and high time-of-flight resolution it is well suited for the investigation of rare heavy PUIs. The crucial disadvantage of this sensor is that due to an instrumental defect, it ceased nominal operation on day 230 in 1996 after collecting only about 150 days of usable data.

The thesis starts with an introduction into PUIs in the heliosphere. After that the SOHO mission, the CELIAS detector package and especially the CTOF sensor are described and the measurement principle of CTOF is explained. Then the in-flight calibration of CTOF and the resulting conversion algorithm from energy-per-charge and time-of-flight into mass-per-charge values is presented. This algorithm is then used to analyse the data in more detail. First a model predicting the peak shapes of the considered ions in mass-per-charge histograms is developed. This model is applied to perform fits of the corresponding peaks in the histogram from which the inner-source heavy PUI composition and velocity spectra can be derived. The inner source heavy PUI composition is then compared to the solar wind composition measured by ULYSSES/SWICS and the w-spectra are analyzed and discussed.

In the end the findings of this thesis are summarized and an outlook to further research is given.

Zusammenfassung

Diese Master-Arbeit befasst sich mit der Studie von Pickup Ionen, die auf der SOlar and Heliospheric Observatory (SOHO) Sonde mithilfe des Charge Time-Of-Flight (CTOF) Sensors, der Teil vom Charge, ELement and Isotope Analysis System (CELIAS) ist, bei 1AU gemessen wurden. Pickup Ionen (PUI) entstehen aus Neutralteilchen innerhalb der Heliosphere durch Photoionisation, Ladungsaustausch mit Sonnenwindprotonen oder Elektronenstößen und beginnen dann mit dem Sonnenwind zu interagieren. Man kann sie durch ihren niedrigen Ladungszustand und ihre suprathermale Geschwindigkeitsverteilung von gewöhnlichen Sonnenwindionen unterscheiden. Die Neutralteilchen können einerseits aus dem interstellaren Medium oder einer inneren Quelle, die momentan noch nicht vollständig verstanden ist, stammen.

CTOF ist ein Flugzeit-Massenspektrometer und bestimmt die Masse, Masse-pro-Ladung und Energie eines einfallenden Ions mithilfe der kombinierten Messung von Energie-pro-Ladung, Flugzeit und restlicher Energie. Da der Geometriefaktor verhältnismäßig groß und die Flugzeit-Auflösung sehr gut ist, eignet sich dieser Sensor hervorragend, um PUI zu untersuchen. Ein Nachteil des Instruments ist, dass aufgrund eines technischen Defekts nur ein limitierter Datensatz von ungefähr 150 Tagen zur Verfügung steht.

Die Arbeit beginnt mit einer kurzen Einführung über PUI in der Heliosphäre. Danach werden die SOHO Mission, das CELIAS Experiment und natürlich der CTOF Sensor vorgestellt, wobei insbesondere das Messprinzip von CTOF im Detail erklärt wird. Es wird eine in-flight Kalibration des Sensors durchgeführt, was bedeutet dass ein Algorithmus, der Energie-pro-Ladungs- und Flugzeitdaten in Masse-pro-Ladungs Werte umrechnet, aus den Messdaten des Sensors hergeleitet wird. Anschließend wird dieser Algorithmus benutzt, um die Messdaten auszuwerten. Zunächst wird ein Modell für die Peak-Formen verschiedener PUI in Masse-pro-Ladungs Histogrammen entwickelt. Dieses wird dafür benötigt die entsprechenden Peaks in den Histogrammen zu fitten, womit die Komposition der PUI, die aus der inneren Quelle stammen, abgeschätzt wird und Geschwindigkeitsverteilungen abgeleitet werden. Die Komposition wird schließlich mit der von ULYSSES/SWICS gemessenen Sonnenwindkomposition verglichen und ein neuer Ansatz zur Erklärung der Geschwindigkeitsverteilungen wird vorgestellt.

Chapter 1

Pickup Ions

Pick**U**p **I**ons (PUI) form from neutral atoms in the heliosphere that are ionized and subsequently interact with the solar wind and the heliospheric magnetic field, respectively. The neutral atoms originate from the interstellar medium or from an incompletely understood source in the inner heliosphere. For the latter multiple possible production scenarios have been proposed, but none of them can explain all observed characteristics in sufficient detail.

1.1   General Processes

A neutral atom in space does not feel any electromagnetic forces that are exerted by the solar wind. This changes immediately when the neutral particle is ionized by processes such as photoionization, charge-exchange with solar wind protons or, with a smaller probability, electron impact ionization. Then the freshly created PUI is accelerated by the solar wind convection E-field and begins to gyrate around the frozen-in heliospheric magnetic field that is swept along with the solar wind. There are three characteristics that help to distinguish between solar wind and pickup ions. To start with, in contrast to solar wind ions, that are usually highly charged, PUIs are mostly single-charged, because once ionized they are rapidly transported to regions with lesser **E**xtreme **U**ltra-**V**iolet (EUV) photon and solar wind proton flux leading to a decreasing probability for a second ionization. Secondly, the PUI density in the heliosphere can have specific spatial distributions (as discussed in sec. 1.2 or 4.3). Furthermore the pickup process manifests itself in a specific, suprathermal velocity distribution function. As neutral atoms do not interact with the solar wind convection E-field, they may have different speeds relative to the solar wind. The initial velocity of a freshly created PUI consists of a superposition of the gyration around the B-field and the acceleration of the guiding center to solar wind speed by the convection E-field. Thus the initial ve-

locity distribution is a ring-distribution in velocity space with a gyro-radius which depends on the present magnetic field configuration and the speed of the solar wind. As the resulting velocity depends on the present solar wind velocity, it is useful to consider the ratio of solar wind and PUI speed:

$$w = \frac{v_{ion}}{v_{sw}}. \tag{1.1}$$

This quantity is also used to investigate PUI velocity spectra. In fig. 1.1 a so-called
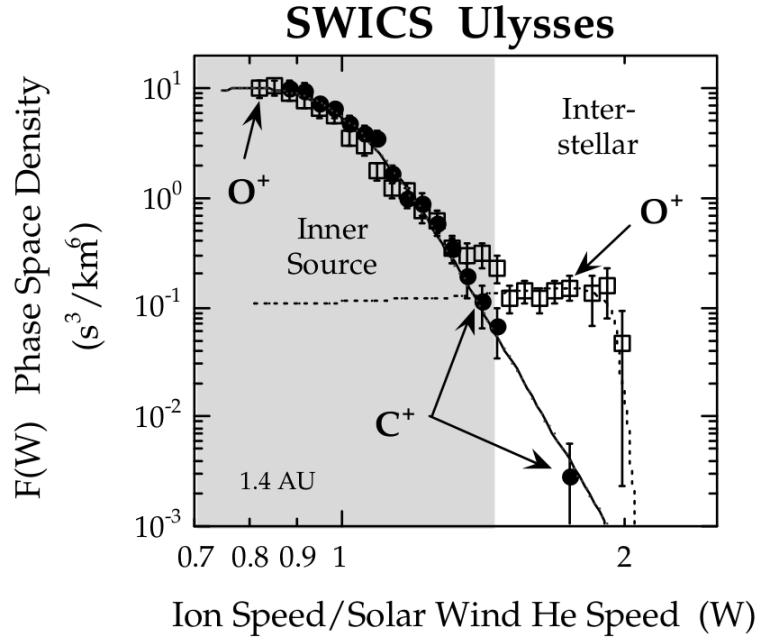
Figure 1.1: Velocity spectrum for C^{1+} and O^{1+} expressed in terms of w. The distributions show different shapes due to the different origin of the PUI. The figure was taken from Gloeckler and Geiss (1998).

w-spectrum for C^{1+} and O^{1+} measured with ULYSSES/SWICS by Gloeckler and Geiss (1998) is shown. The figure is split into two areas, indicating the two different origins of PUIs, that are introduced in the next sections.
The further interaction of the freshly created ions and the solar wind is not completely understood. Vasyliunas and Siscoe (1976) assumed that PUIs are immediately isotropized by rapid pitch-angle scattering on magnetic fluctuations (resonant wave-particle interactions, cf. Tsurutani and Lakhina (1997)), thus rapidly forming an isotropic shell distribution in velocity space. Oka et al. (2002) found that the mean-free-paths of PUIs and therefore the timescales for pitch-angle scattering are larger than assumed. Saul et al. (2007) suggest that pitch-angle scattering

through 180°may work efficiently. Recently Drews et al. (2013) showed that the PUIs velocity distribution is superimposed by an anisotropic beam corresponding to freshly injected PUI.

After the PUIs have been injected they are believed to be adiabatically cooled (Vasyliunas and Siscoe, 1976). The PUIs are bound to the expanding solar wind and hence it is assumed that their velocity distribution shrinks when travelling outwards similar to an expanding ideal gas. But the micro-physical mechanisms causing this are not understood in detail and it is "in some ways remarkable, that the pickup ion population, a non-Maxwellian unstable distribution in a collisionless plasma, could cool in a similar manner to the thermodynamics of a dense gas" (Saul et al., 2009). One must always keep in mind that these theories rely on assumptions that must not necessarily be justified.

1.2   Interstellar Pickup Ions

One possible source for neutral particles in the heliosphere is the interstellar wind that is caused by the motion of the heliosphere through the interstellar medium. Charged particles are prevented from entering the heliosphere by the magnetic barrier formed by the heliosheath, but neutral particles can enter freely and are only affected by the forces of gravity and radiation pressure. This leads to the formation of two regions with an enhanced density of neutral particles, one on the upwind side and one on the downwind side of the sun with respect to the interstellar wind (see fig. 1.2). The focusing cone on the downwind side is due to gravitational focusing of the neutral particle trajectories. It was first observed in-situ by Möbius et al. (1985). It is pronounced for elements having a high **F**irst **I**onization **P**otential (FIP), because elements with low FIPs are readily ionized and strongly depleted before reaching this region. On the upwind side of the sun the so-called crescent (Drews et al., 2012) can be found, which means that a spacecraft orbiting the sun with a constant radial distance sees a local maximum of PUI density when passing the upwind side of the sun. This effect can be explained by considering differences in the pathway of interstellar neutrals. Neutrals that had a longer pathway before reaching the spacecrafts radial distance from the sun were exposed longer to the sun's EUV radiation. Thus the probability for these neutrals to reach the spacecraft's radial distance is lesser than for neutrals with a shorter pathway. This region is more pronounced for elements having an intermediate FIP like Oxygen, for which this structure was observed by Drews et al. (2012).

Interstellar PUI also shows a specific velocity distribution. The inflow velocity of the interstellar wind is about $v_{\text{LISM}} \approx 26\frac{\text{km}}{\text{s}}$. Thus, one can consider these ions to be at rest compared to the solar wind ($v_{sw} \approx 300-800\frac{\text{km}}{\text{s}}$), which means that they have approximately solar wind speed in the reference frame of a solar wind particle.
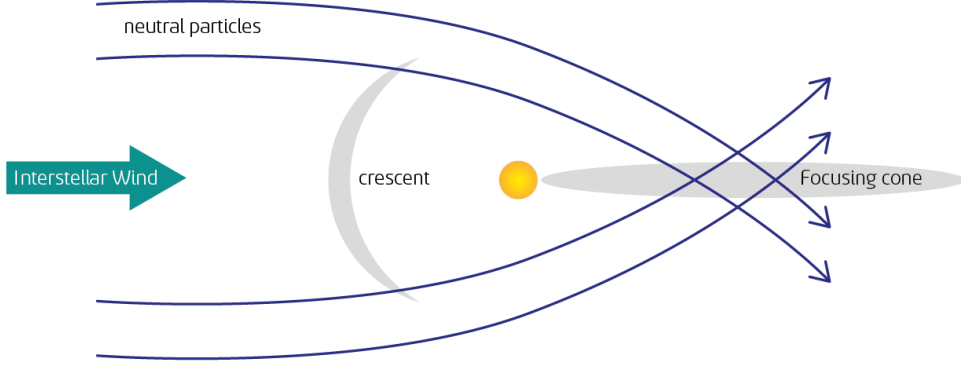
Figure 1.2: Sketch of the heliosphere showing the position of the focusing cone and the crescent of PUI evolving from the inflow of the interstellar wind.

Assuming a perpendicular magnetic field configuration a PUI then gyrates with solar wind speed when ionized. From these simple considerations it is clear that the maximum speed a PUI can have is approximately twice the solar wind speed, which results in a sharp cutoff at $w = 2$ in PUI w-spectra. This can be seen in fig. 1.1, where a w-spectrum for O^{1+} that was derived from ULYSSES/SWICS measurements by Gloeckler and Geiss (1998) is shown, for instance.

1.3 Inner-source Pickup Ions

Apart from the interstellar source, there has to be a source for neutral particles inside the inner heliosphere (Geiss et al., 1995). One indication for that is that the amount of measured O^{1+} ions resembles the amount of C^{1+} ions at $w \approx 1$, while there is only 0.03% of carbon, but 81% of oxygen its neutral state in the interstellar medium (Frisch et al., 2011). Much of the EUV radiation that could ionize oxygen is filtered out before reaching the interstellar medium, because the FIP of oxygen (13.62eV) is only slightly bigger than the FIP of hydrogen (13.60eV). Furthermore significant differences in the velocity distribution of O^{1+} and C^{1+} were measured

Element	Inner source	Solar wind
C	1.46 ± 0.12	0.683 ± 0.040
N	0.40 ± 0.05	0.111 ± 0.022
O	$\doteq 1$	$\doteq 1$
Ne	0.32 ± 0.05	0.082 ± 0.013
Mg	0.49 ± 0.15	0.105 ± 0.025
Si	0.32 ± 0.12	0.115 ± 0.023

Table 1.1: Elemental composition of the inner source PUI and the solar wind as ratios of the Oxygen-abundance. The table is based on the table used in Allegrini et al. (2005) with the PUI composition values from Gloeckler et al. (2000) and the solar wind composition values taken from von Steiger et al. (2000) that were derived for a fast stream from a South Polar coronal hole.

and it looks as if the C^{1+} ions and a fraction of the O^{1+} ions seem to be almost thermalized with the solar wind at 1AU (Schwadron et al., 2000). The inner source has been studied for about two decades now and the following characteristics have been revealed that are summarized by Allegrini et al. (2005):

Solar wind composition:
In table 1.1 the relative elemental abundances of the inner source PUI (Gloeckler et al., 2000) and the solar wind (von Steiger et al., 2000) measured with ULYSSES/SWICS are listed. In the original work of Gloeckler et al. (2000), the elemental abundance ratios were normed to the abundance of neon. Then the ratios of inner-source N^{1+}/Ne^{1+}, Mg^{1+}/Ne^{1+} and Si^{1+}/Ne^{1+} are the same as the solar wind abundance ratios within the error bars. But due to its very high FIP, neon has a very pronounced contribution of interstellar PUIs that interfere the measurement of the inner-source abundance. Therefore the elemental abundance ratios were normed to the abundance of oxygen, where strong deviations from the solar wind composition can be found. However, the existence of inner-source Ne^{1+} already suggests that the solar wind is somehow involved in the production of inner-source neutrals. Neon is a very volatile element that does not occur in interplanetary dust grains or comets and thus it is very likely that the solar wind itself is the source for these inner-source PUIs.

Peak near the sun: Assuming adiabatic cooling one can calculate from inner source PUI velocity spectra that the peak of ion production must lie in the range of $10 - 50 R_{\odot}$ (Schwadron et al., 2000).

PUI flux: From ULYSSES/SWICS measurements Geiss et al. (1996) calculated

a production rate of $\sim 2 \cdot 10^6 \frac{\mathrm{g}}{\mathrm{s}}$. Any scenario describing the production of inner source PUI must be able to explain this production rate.

Randomly distributed source: The time between two counts of PUIs is given by a Poisson distribution, which implies that the inner source PUI are produced randomly in time (Geiss et al., 1996). If there were local point sources, one would expect a deviation of this distribution in such a way, that there would be far more counts following close to each other.

Stability over solar cycle: Allegrini et al. (2005) showed that the flux of PUI is similar during solar minimum and maximum. This means that the production of inner source PUI is not affected by coronal mass ejections or other solar-maximum related phenomena.

Note that these characteristics were derived from measurements which had very low counting statistics. Thus, one should treat these points listed above with caution and a little doubt and scepticism might not be inappropriate.

Possible production scenarios have to be investigated in the context of these characteristics. To date 4 scenarios have been proposed:

1. Solar wind recycling (Schwadron et al., 2000; Gloeckler et al., 2000)

2. Solar wind neutralization and charge exchange (Wimmer-Schweingruber and Bochsler, 2003)

3. Sungrazing comets (Bzowski and Królikowska, 2004)

4. Dust-dust collisions (Mann and Czechowski, 2005)

Schwadron et al. (2000) and Gloeckler et al. (2000) posit that μm-sized dust grains are immersed in the solar wind and many solar wind particles are implanted into the surface of these grains until they are saturated. Then these particles are reemitted (thermally or by solar wind sputtering) from the dust grains as neutral atoms or molecules. These former solar wind ions can then again be ionized. In this scenario a similar composition to the solar wind can be achieved. However there should be a substantial enhancement of grain material from sputtering of the grain surface (Wimmer-Schweingruber and Bochsler, 2003). Schwadron et al. (2000) also estimated that the total geometric dust cross-section required to reach a PUI flux as high as observed. They found that it would be orders of magnitude larger than the total geometric dust cross-section deduced from zodiacal light measurements (Allegrini et al., 2005), which is an argument against the validity of this scneario.

The solar wind neutralization scenario again involves small dust grains (Wimmer-Schweingruber and Bochsler, 2003). Collisions form very small grains whose diameter is on the order of the penetration length of solar wind ions. This means that ions colliding with these grains pass through and exit the grain again as neutrals, singly or low charged ions. The difficult point in this scenario is the stability of PUI flux over the solar cycle, because nm-sized dust particles are supposed to be trapped inside coronal mass ejections which would affect the PUI flux in solar maximum (Allegrini et al., 2005).

Bzowski and Królikowska (2004) propose that the 60-120 sungrazing comets per year that can be observed with SOHO/LASCO are responsible for the inner source PUIs. Their mass is transferred into the solar wind as PUIs because they disintegrate very close to the sun. However, within this model a very local production of PUI would be expected and the elemental composition of sungrazing comets is not expected to match the solar wind composition.

The latter point is also the problem in the scenario of dust-dust collisions (Mann and Czechowski, 2005). Interplanetary dust particles are also not expected to contain volatile elements like neon, which is observed as inner source PUI.

None of the proposed scenarios introduced above can explain all observed characteristics of the inner source PUI. But note that there are quite big uncertainties in both the characteristics of inner source PUI and the implications of the proposed models. Therefore, inner-source PUIs merit more detailed investigation. This is the key motivation for this Thesis work.

1.3.1 Ionization rates

When considering the production of PUIs one has to take into account that different ions have different ionization cross-sections and therefore different ionization rates. In this work we only consider photoionization due to this being the dominating ionization process for PUIs.

The photoionization cross-sections, ν, were calculated by Berger using the Python script `ionisationrates.py` (personal communication, Nov. 2013). In this script measurements of the TIMED spacecraft are used to estimate the sun's EUV flux during solar minimum conditions, which is comparable to the flux in the investigated time period. Then cross-sections for photoionization are calculated following the formula and parameters given in Verner et al. (1996). In table 1.2 the calculated ratios of the photoionization cross-sections normed to oxygen are listed. The meaning of these values is explained on a short example:

Let there be neutral C and O atoms of the same amount in the interplanetary medium that are irradiated by sun. Then due to the larger photoionization cross-section of C, the ionization of a C atom is more probable than the ionization of an O atom. Thus, we would expect the ratio of ionized particles to be $\frac{C^+}{O^+} = 2.54$.

Element	$\frac{\nu(\text{Ion})}{\nu(\text{O})}$
C	2.54
N	1.03
O	$\doteq 1$
Ne	0.69
Mg	1.63
Al	494.98
Si	77.84

Table 1.2: Ratios of the photoionization cross-sections of neutral atoms in the interplanetary medium in solar minimum conditions derived by Berger (personal communication, Nov. 2013).

Chapter 2

Instrumental Background

2.1 The SOHO mission

2.1.1 Overview

The **SO**lar and **H**eliospheric **O**bservatory (SOHO) is a joint project of the **E**uropean **S**pace **A**dministration (ESA) and the **N**ational **A**eronautics and **S**pace **A**dministration (NASA) "to study the sun from its interior to, and including, the solar wind in interplanetary space" (Fleck, 1995). Its main scientific objectives are to investigate:

1. the structure and dynamics of the solar interior,

2. the formation and heating of the solar corona and

3. the origin and acceleration of the solar wind.

For this aim 12 instruments were mounted on the SOHO spacecraft, that was launched on 2$^{\text{nd}}$ December 1995. It was brought into a halo orbit around the First Lagrangian Point, L1, situated at the earth-sun line in a distance of about 1.5· 10^6 km from the earth. At this distance the spacecraft is always outside earth's magnetosphere, which is required for in-situ measurements of the solar wind. The spacecraft is three-axis stabilised and permanently points towards the sun.
The nominal operational lifetime was 2 years, but the mission has been extended 5 times. SOHO is still in operation today with plans to continue till 2016.

2.1.2 Scientific Payload

One can distinguish between three groups of instruments aboard the SOHO spacecraft that roughly correspond to the three main scientific objectives of the mission as listed in sec. 2.1.1:

1. Helioseismology instruments: GOLF, VIRGO and MDI/SOI

2. Solar atmosphere remote sensors: SUMER, CDS, EIT, UVCS, LASCO and SWAN

3. Solar wind in-situ instruments: CELIAS, COSTEP and ERNE

More information about the SOHO mission is given in Fleck (1995).

2.2 CELIAS

2.2.1 Overview

The **C**harge, **El**ement and **I**sotope **A**nalysis **S**ystem (CELIAS) is a suite of three **T**ime-**of**-**F**light (ToF) spectrometers and an **E**xtreme **U**ltra-**V**iolet (EUV) sensor that is completed by a **D**ata **P**rocessing **U**nit (DPU)(Hovestadt et al., 1995). Its main scientific objectives are the determination of:

1. the isotopic composition of the solar wind,

2. the elemental and ionic composition of the solar wind,

3. the composition and energy distribution of suprathermal particles and

4. the composition of interstellar pickup-ions.

2.2.2 CELIAS sensors

Each of the CELIAS ToF-spectrometers (CTOF, MTOF and (H)STOF) combines electrostatic deflection and ToF measurement. Additionally the residual energy is measured in CTOF and STOF. In the following subsections the sensors are briefly introduced. The CELIAS sensor package is summarized by Hovestadt et al. (1995) in more detail.

CTOF

The **C**harge determining **ToF** sensor (CTOF) is able to determine the mass, charge and speed of ions. This sensor focusses on the determination of the ionic composition and energy distribution of solar wind ions.
Unfortunately the sensor ceased nominal operation on **D**ay **O**f **Y**ear (DOY) 230, 1996, due to the failure of critical electronic components. Thus, only a limited amount of data is available.

The energy range is roughly limited to 0.3keV/Q to 35keV/Q due to the electrostatic deflection (see sec: 2.3.1). This corresponds to a speed range of about $200\frac{\text{km}}{\text{s}}$ to $1800\frac{\text{km}}{\text{s}}$ for He^{2+} or $150\frac{\text{km}}{\text{s}}$ to $1500\frac{\text{km}}{\text{s}}$ for O^{6+}, which means that the full solar wind speed range ($\sim 300\frac{\text{km}}{\text{s}}$ to $800\frac{\text{km}}{\text{s}}$) is easily covered for these typical solar wind ions.

A detailed description of the sensor is given in sec. 2.3.

MTOF

The **M**ass determining **ToF** sensor (MTOF) aims to measure the isotopic composition of the solar wind. The required high mass resolution is provided by a special arrangement of electrodes. The oscillation period of an ion in the potential of a harmonic oscillator, in which the electric field increases linearly with distance, does not depend on its energy. This configuration leads to a ToF that only depends on the **M**ass-**p**er-**C**harge (MpQ) of the ion and no **E**nergy-**p**er-**C**harge (EpQ) information is required, which allows MTOF's entrance system to have a broad EpQ passband.

Furthermore a **P**roton **M**onitor (PM) is included in the MTOF sensor, that provides information about the solar wind speed, density and direction.

(H)STOF

The **S**uprathermal **ToF** sensor (STOF) is divided into two sections covering different energy ranges: STOF main and HSTOF. These sections differ in the shape of their electrostatic deflection units and share one ToF section. In general (H)STOF operates similarly to CTOF, but works without post-acceleration and covers a higher energy range (20keV/Q to 4000keV/Q). This energy range closes the energy gap between solar wind and energetic particle instruments, like ERNE and COSTEP.

SEM

The **S**olar **E**UV **M**onitor (SEM), basically consisting of a diffraction grating and three light diodes, measures permanently the intensity of EUV radiation in the wavelength range of 17nm to 170nm. With this measurement correlations between pickup-ion abundances and solar EUV radiation can be investigated.

2.3   The CTOF sensor

2.3.1   Measurement sections

CTOF is able to measure an ion's EpQ, ToF and residual energy. In fig. 2.1 the path of an ion through the sensor is sketched. First the electrostatic deflection unit must be passed, after that the ToF and energy measurements follow. In the following the particular measurement sections are introduced.

If an ion triggers all three measurements one speaks of a triple coincidence and the energy, MpQ and mass of the ion can be deduced. But it can happen that only a ToF measurement is triggered. Then one speaks of a double coincidence and only the speed and MpQ of the ion can be determined.
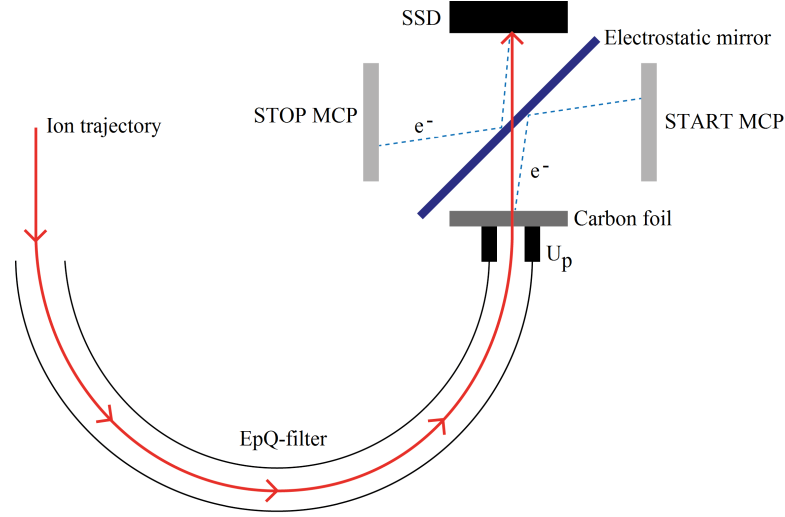

Figure 2.1: Schematic illustration of the CTOF sensor. The red line indicates an ion's trajectory through the sensor passing all measurement sections.

Electrostatic deflection

After an ion enters the sensor through its entrance ion optic system, that spans a solid angle of 30°×50°, it has to pass the electrostatic deflection system. The main part of this system is a 180° hemispherical capacitor. By applying a voltage on this capacitor incoming ions are forced on a curved trajectory. Only ions that satisfy the condition that the curvature of their trajectory is equal to the curvature of the capacitor (with a small tolerance range) can pass. With the following equations one can show that this system serves an an EpQ filter. The electrostatic force must be equal to the centripetal force of the curved trajectory to fulfill the condition

above:

$$
\begin{aligned}
q_i \mathcal{E}_c &= \frac{m_i v_0^2}{r_c} \\
\Leftrightarrow q_i \frac{U_c}{d} &= \frac{2E_{kin}}{r_c} \\
\Leftrightarrow \frac{E_{kin}}{q_i} &= \frac{U_c r_c}{2d}
\end{aligned}
\tag{2.1}
$$

Here q_i, m_i and v_0 denote an ion's charge, mass and velocity. From the latter two the kinetic energy E_{kin} follows. The curvature radius of the capacitor is denoted as r_c. The electric field strength $\mathcal{E}_c$ can be locally approximated by the field strength of a plane capacitor: $\mathcal{E}_c \approx \frac{U_c}{d}$, where U_c is the applied voltage and d the distance between the capacitor plates. One can see in eqn. 2.1 that the EpQ of passing ions solely depends on the applied voltage, because d and r_c are constants of the instrument.

The applied voltage can have 116 values that are stepped through in a cycle of about 5 minutes from high EpQ to low EpQ values. Consequently every voltage value lasts for approximately 2.6 seconds. In Aellig (1998) the following relation between step-number j and EpQ value $U_j = \left(\frac{E_{kin}}{q_i} \right)_j$ is given:

$$
U_j = U_0 r^{s_{max} - j} \ .
\tag{2.2}
$$

The parameters used are:

- The minimum EpQ value $U_0 = 0.331095$kV,

- the maximum step-number $s_{max} = 116$ and

- the scaling factor $r = 1.040926$.

From eqn. 2.2 the energy range that is covered by CTOF can be deduced. It is dependent on the ion's charge q_i and reaches from $E_{kin,min} = q_i \cdot 0.331$kV to $E_{kin,max} = q_i \cdot 34.725$kV. For singly ionized PUI this means that the energy range from 0.331keV to 34.725keV is covered.

One great advantage of the CTOF sensor is, that the cycle of the electrostatic deflection unit can be interrupted in the case of very high proton fluxes that would be likely to destroy detector components. Protons are the most abundant ions in the solar wind, approximately 25 times as abundant as He^{2+} ions, and 1000-1500 more abundant than Oxygen ions. This allows the sensor to have such a large geometry factor, which increases the counts of heavy ions in the solar wind.

ToF section

After passing the electrostatic deflection the ions are post-accelerated by a high voltage U_p and hit a carbon foil, that represents the entrance to the ToF section of the sensor. After the ions have been post-accelerated they have the following energy:

$$E_{post} = \left(\frac{E_{kin}}{q_i} + U_p \right) q_i \qquad (2.3)$$

The foil has an area density of $\rho = 2.5 \frac{\mu g}{cm^2}$ (Hefti, 1997) corresponding to a thickness of $f \approx 200 \text{Å}$. By passing the foil the ions loose a part to all of their charge and secondary electrons are emitted from the foil. These secondary electrons are then guided by an electrostatic mirror towards a **M**icro**C**hannel **P**late (MCP) that triggers the START signal of the ToF measurement. After a distance of $d = 70.5$mm a **S**olid **S**tate **D**etector (SSD) is placed, where also secondary electrons are emitted when hit by an ion. These secondary electrons are then again guided by the same electrostatic mirror towards another MCP that triggers the STOP signal of the ToF measurement.

Energy measurement

The measurement of the ion's residual energy is performed in the SSD. A SSD, also known as semiconductor detector, is basically a diode that is reverse biased so that a depletion zone evolves in the p-n junction. Energetic particles passing through the depletion zone create electron-hole pairs that are pulled to the electrodes by the present electric field. The resulting charge pulse is proportional to the dissipated energy of the particle in the detector. The measured energy of the SSD is not the same as the energy of the impinging ion due to different effects, for example the creation of phonons in the crystal. Therefore the parameter $\beta(i, E_{tot})$ is introduced that depends on the ion species i and impact energy, that links the particle's energy E_{tot} and the measured energy E_{SSD} by

$$E_{SSD} = \beta(i, E_{tot}) E_{tot} \ . \qquad (2.4)$$

The SSD inside CTOF consists of doped Silicon and is of circular shape with a radius of $r_{SSD} = 25$mm (Aellig, 1998). Its detection threshold was set to ~ 25keV well above the system's electronic noise.

All relevant intrumental parameters taken either from Aellig (1998) or Hovestadt et al. (1995) are summarized in table 2.1.

Electrostatic deflection		
Quantity	Meaning	Value
U_0	Minimum EpQ value	0.331095kV
s_{max}	Maximum step number	116
r	scaling factor	1.040926
ΔEpQ	EpQ bandwidth	5.5%
ToF section		
U_p	post-acceleration voltage	$\begin{cases} 18.83\text{kV for DOY } 82-145 \\ 22.69\text{kV for DOY } 150-230 \end{cases}$
ρ	area density of the carbon foil	$2.5\frac{\mu\text{g}}{\text{cm}^2}$
l_τ	ToF pathlength	70.5mm
Energy measurement		
r_{SSD}	radius of the SSD	25mm
U_{thresh}	detection threshold	< 25kV

Table 2.1: Instrumental parameters of the CTOF sensor divided into the single measurement sections. The values have been taken from Aellig (1998) and Hovestadt et al. (1995). The values for U_p were taken from CTOF's housekeeping data.

2.3.2 Principle of detection

As stated in sec. 2.2.2 the MpQ, mass and speed of impinging ions can be determined with CTOF. Because one can identify an ion by its MpQ and mass it is possible to create velocity or energy spectra, respectively, for specific ion species from CTOF's measurements.

For the determination of the ion's MpQ the EpQ and ToF information is sufficient. Let E_{kin} be the kinetic energy of an ion in space with the mass m_i and charge q_i. The electrostatic deflection unit can only be passed if the ion's EpQ equals the right-hand-side of eqn. 2.1 with the applied voltage U_c (see sec. 2.3.1). Then the ion is post-accelerated by the voltage U_p and passes the carbon foil loosing some of its energy. This is taken into account by introducing the factor $\alpha(i, E_{post}) = \frac{\Delta E}{E_{post}}$ representing the ratio of the part of the energy that is deposited, ΔE, and the ion's energy after post-acceleration, E_{post}. Thus the total energy E_{tot} of the ion in the ToF section can be expressed as:

$$E_{tot} = \left(\frac{E_{kin}}{q_i} q_i + U_p q_i \right) \left(1 - \alpha(i, E_{post}) \right) = \frac{m_i}{2} v_i^2. \tag{2.5}$$

Note that $v_i (\neq v_0)$ (cf. eqn. 2.1) is the ion's velocity in the ToF section and not in space. This velocity can now be calculated to:

$$v_i = \sqrt{\frac{2q_i}{m_i}\left(\frac{E_{kin}}{q_i} + U_p\right)(1 - \alpha(i, E_{post}))}. \tag{2.6}$$

With the ToF pathlength $l_\tau = 70.5$mm the ToF τ can be determined, from which the MpQ can be derived:

$$\tau = \frac{l_\tau}{v_i} = \frac{l_\tau}{\sqrt{\frac{2q_i}{m_i}\left(\frac{E_{kin}}{q_i} + U_p\right)(1 - \alpha(i, E_{post}))}} \tag{2.7}$$

$$\Rightarrow \frac{m_i}{q_i} = 2\frac{\tau^2}{l_\tau^2}\left(\frac{E_{kin}}{q_i} + U_p\right)(1 - \alpha(i, E_{post})) \tag{2.8}$$

Once the MpQ is known, the original velocity, v_0, of the ion can directly be determined from the EpQ measurement:

$$E_{kin} = \frac{E_{kin}}{q_i} \cdot q_i = \frac{m_i}{2}v_0^2 \tag{2.9}$$

$$\Rightarrow v_0 = \sqrt{\frac{2\frac{E_{kin}}{q_i}}{\frac{m_i}{q_i}}} \tag{2.10}$$

For the calculation of the mass the residual energy measurement is needed. As mentioned in sec. 2.3.1 not the whole energy of the particle is measured, because of the creation of phonons that do not contribute to the SSD signal and the influence of the deadlayer of the SSD (see eqn. 2.4). With this in mind the expression

$$m_i = \frac{2E_{tot}}{v_i^2} = \frac{\tau^2}{l_\tau^2}\frac{E_{SSD}}{\beta(i, E_{tot})} \tag{2.11}$$

can be derived. The ToF τ can be calculated with eqn. 2.7. From the MpQ and mass the charge of a particle can be deducted and finally the particle can be identified.

The formulae above must be understood as idealized equations. A significant problem are the parameters α and β. Both depend on the ion species and the ion's energy and represent an energy loss. The stopping of fast particles in matter is a process with statistical character (Ziegler et al., 2010), which means that two ions of the same species and the same energy might have different energy depositions. So the parameters must be regarded as the most probable energy loss, what complicates the determination of the MpQ and mass. A more detailed treatment of this problem will be given in sec. 3.2.

2.3.3 Data products

The DPU collects the measured EpQ, ToF and residual energy information, pre-processes it and creates various data products, that are transmitted to ground. These data products are:

1. Summary rate data,

2. Spectral Matrix Rates (SMR),

3. Matrix Element Rate (ME) and

4. Pulse-height analysis data (PHA).

Furthermore there is the housekeeping data, that provides information about the status of the instrument, for example the current post-acceleration voltage or instrument temperature.

For the SMR and ME data, the DPU uses numerical approximations of the MpQ and mass, M (see eqn. 2.8 and 2.11), and sorts the events in an MpQ-M matrix. This procedure allows a quick analysis of the data, but the compression of the data in MpQ-M matrices goes along with a loss of information.

Therefore the PHA data is used in this work, that contains the EpQ (in step numbers), ToF and residual energy information (both in channel numbers) for every transmitted event. A maximum of 32 events per cycle is transmitted for every EpQ-step. This means that events have to be selected using a priority scheme, if more events are measured in this cycle. But this thesis deals with the study of rare HPUI that never reach fluxes exceeding 32 counts/cycle. Therefore this priority scheme can be neglected.

As the EpQ, ToF and residual energy information is given in channel numbers and there are no reliable conversion algorithms an in-flight calibration is required for the analysis of the PHA data. This calibration is done in the next chapter.

2.3.4 Detection efficiencies

The detection efficiency for an ion entering the sensor with a given energy E is the product of some single probabilities. As the ToF and EpQ measurement is sufficient for the investigation of HPUIs, only a ToF measurement has to be triggered to detect such an ion. Therefore, only the double-coincidence efficiency is considered, although the energy measurement has also a limited efficiency, of course.

First the scattering angle of the ion after passing the carbon foil must be smaller than $\gamma_0 = 19.5°$. Otherwise the ion is lost at the detector walls and no secondary electrons are emitted that could trigger a STOP pulse for the ToF measurement. Let the probability for an ion to have a scattering angle $\gamma < 19.5°$ be p_γ. It is

dependent on the ion species and the energy of the ion after post-acceleration. Then there are the probabilities, if a START or STOP signal is triggered by the MCPs, p_{start} and p_{stop}. These depend on the yield of secondary electrons that are emitted by the surfaces, which depends on the impact energy of the ion.

Finally the product of these probabilities gives the probability of a ToF measurement:

$$p_{\text{ToF}} = p_\gamma \cdot p_{start} \cdot p_{stop} \tag{2.12}$$

All probabilities somehow depend on the ion's energy when entering the sensor. Thus, the double-coincidence efficiency also depends on this. Generally the detection eficiency increases with increasing energy.

A more sophisticated model for the double-coincidence detection efficiency of CTOF has been developed by Aellig (1998). In fig. 2.2 his modeled efficiencies for iron, argon, oxygen and helium are shown together with calibration data. Especially for iron, argon and oxygen the double coincidence efficiency increases strongly when increasing the ion's energy from 1keV/amu to about 10keV/amu. After that the efficiency seems to approach a limit. It is to be expected that the efficiencies of all ion species behave approximately like this.
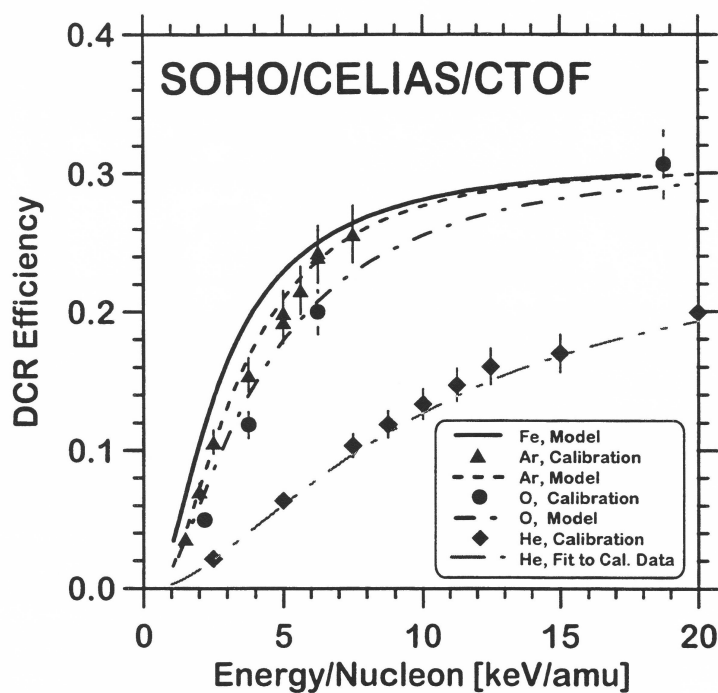

Figure 2.2: Models and calibration data for the double-coincidence efficiency of CTOF taken from Aellig (1998).

18

Chapter 3

Calibration

In this chapter a calibration of the ToF information from the PHA data is performed. Conversion functions from channel numbers to physical units and from the EpQ and ToF to MpQ values, respectively, are deduced from flight data of CTOF. The in-flight calibration of the residual energy information and an algorithm for the determination of an ion's mass can be found in the work of Janitzek (2014) that evolved in close collaboration with this work.

The general idea is to identify ion peaks in the E-T matrices (sec. 3.1.1) or ToF histograms (sec. 3.1.2), respectively, and find their ToF positions for several EpQ-steps. These positions can then be compared with eqn. 2.7 which is a physical model for the ToF position. In that equation the energy loss of the ions in CTOF's carbon foil plays a role. It can be estimated by TRIM simulations. TRIM (**T**ransport and **R**ange of **I**ons in **M**atter) is an established software tool for the calculation of the energy deposition of ions in matter using a Monte-Carlo simulation (Ziegler et al., 2010). For a good fit of eqn. 2.8 to the data it is necessary to optimize the assumed values for the post-acceleration voltage and the carbon foil thickness. This finally gives a conversion from channels into physical units for the ToF, which is a requirement for converting ToF into MpQ values. One has to note that when converting these values one has to assume the energy loss $\alpha(i, E_{post})$ of a specific ion at the given EpQ-step. Consequently the MpQ is only calculated correctly for the assumed ion and the other MpQ values are shifted according to their real energy loss in the carbon foil. Nevertheless ions with arbitrary MpQs can be identified after that procedure.

19

3.1 Determination of ToF positions

3.1.1 E-T Matrix

The first step towards an in-flight calibration is the creation of 2-dimensional residual energy-ToF histograms of the triple coincidence events for every EpQ step, which we call E-T matrices. For these histograms it is necessary that the measurement of all events was done with the same instrument status. Otherwise the signals of the ions would not always lie in the same positions and no or multiple peaks would appear for one single ion species. In our case this means that the events have to be measured with the same post-acceleration voltage, U_p.
CTOF had two periods with a constant post-acceleration voltage, before it ceased nominal operation on DOY 230 1996, that are given in table 2.1.
In fig. 3.1 the E-T matrix of EpQ step 42 for DOY 150 to 230 is shown. Many peaks belonging to specific ion species can easily be spotted. Due to possible differential nonlinearities of the **A**nalog-**D**igital-**C**onverters (ADCs) two channels were summed to one bin for both the ToF and the residual energy information. The maximum count rate of this E-T matrix is 514 counts to give an impression of
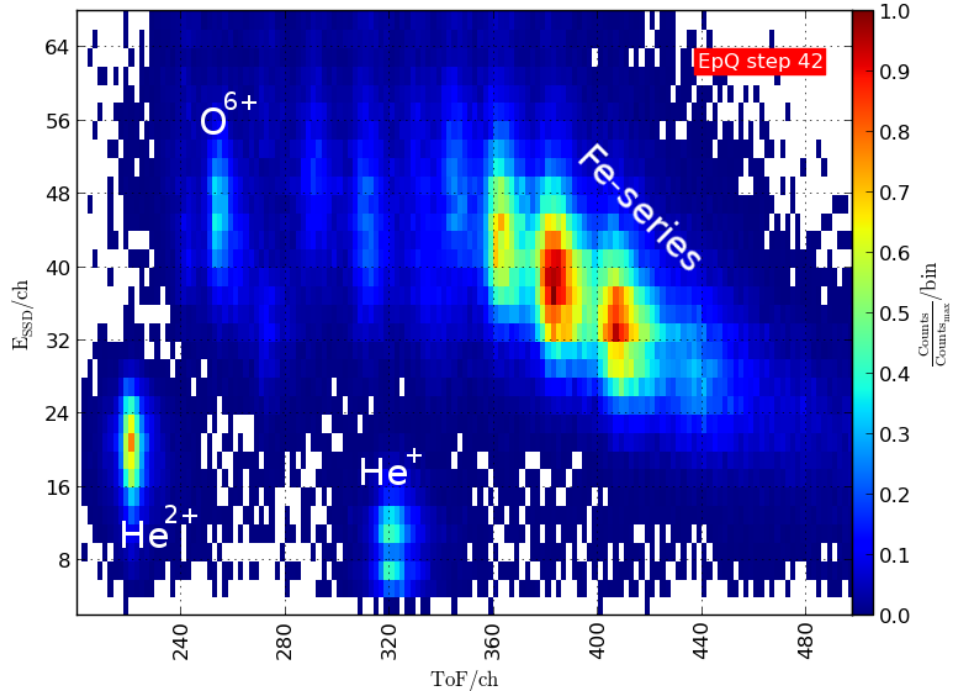

Figure 3.1: E-T matrix of EpQ step 42 for DOY 150 to 230.

the counting statistics. This count rate is reached in the clearly visible iron series. Other dominant solar wind ions that can directly be identified are He^{1+}, He^{2+}, and O^{6+}.

3.1.2 ToF-histograms

Not every ion that triggers a ToF measurement triggers a signal in the SSD. This can happen when the ion's residual energy is below the SSD's threshold or if it does not hit the active area of the SSD. Nevertheless, secondary electrons are emitted in both cases. If the energy measurement did not trigger ($E_{SSD} = 0$) one speaks of a double coincidence and consequently only the EpQ and the ToF information is available for this event.

Especially PUI with masses heavier than helium, which we call **Heavy PUIs** (HPUIs), can be found in the double coincidence data. The maximum energy that is covered by CTOF for these ions is ~ 35keV, which is increased to ~ 55keV by the post-acceleration voltage. At such a low energy, the energy loss in the carbon foil is rather high ($\alpha \approx 15 - 20\%$, see sec. 3.2), which results in a maximum energy of ~ 45keV for HPUIs. Additionally the ions loose a statistical amount of energy in the dead layer of the SSD. This, and other loss mechanisms, are termed the pulse height defect, which is treated in more detail in Janitzek (2014) for CTOF's SSD. This implies that only some HPUI have enough remaining energy to overcome the threshold of the SSD and trigger an energy measurement. Furthermore ions at such low energies tend to suffer more angular scattering in the carbon foil and therefore a greater amount of ions misses the active area of the SSD. This is why most HPUI are measured as double coincidences.

To find the ToF position of HPUIs one needs to create ToF histograms for every EpQ-step. In fig. 3.2 such a histogram is displayed. Again two ToF channels are colored into one to avoid effects of differential ADC nonlinearities. The peaks of C^{1+} and O^{1+} can easily be spotted. Between the peaks there is probably some N^{1+} that is hidden in the tail of C^{1+}.

Especially in the ToF histograms and when considering HPUI the concept of setting nominal w-filters is very useful. With a given ion species one can easily calculate the velocity of this ion from the EpQ-step. The present solar wind speed is given by the PM measurements of CELIAS. Now we can filter the data for a certain w-range for one ion species, which basically means that we cut out a slice of the ion's velocity distribution (cf. fig. 1.1). The filtered w-range for the used ion is different for other ion species, which means that we cut out a different slice of the w-distribution for other ions. By the sophisticated use of these filters one can significantly reduce the background counts in the considered ToF range. For example one can filter the data for a w value of O^{1+} larger than one: $w_{O^+} > 1$. From fig. 1.1 one can see only a small fraction of the O^{1+} velocity distribution
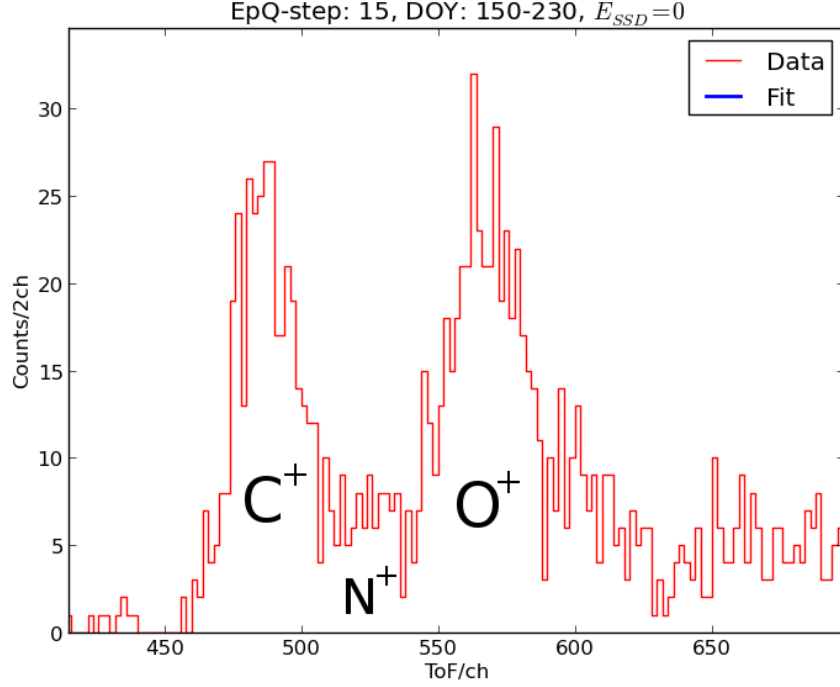
Figure 3.2: ToF histogram of EpQ-step 15 for DOY 150-230. The peaks of C^{1+} and O^{1+} are clearly visible by eye. Between these peaks are probably counts of N^{1+}.

gets filtered out by this condition. But for He^{1+} this filter means $w_{He^+} \gtrsim 2$, which means that only a very small fraction of the He^{1+} distributions can fullfill this condition. The result is, that much background that is caused by the He^{1+} counts is suppressed without affecting the O^{1+} counts in such a great manner.

3.1.3 Fit of the peaks

In both the ET-matrices and the ToF-histograms the most probable ToF position of a certain ion at one EpQ-step can be determined by a fit of the corresponding peak. As the peaks have different shapes and the peak positions might be shifted by neighbouring peaks one has to be careful which fit-function to use to receive a precise result. For the in-fight calibration we used the positions of 7 different ions listed in table 3.1. They can be divided into three groups which require a fit-function.

An example for every group is displayed in fig. 3.3. The peaks of He^{1+} and He^{2+} lie seperated from other peaks in the ET-matrix. Furthermore the energy loss of these ions in the carbon foil follows approximately a Gaussian distribution. We

22

Ions	Fit-function	Plot
He^{1+}, He^{2+}, O^{6+}	2D-Gaussian	ET-matrix
Fe^{10+}, Fe^{11+}	Sum of 5 2D-Gaussians	ET-matrix
C^{1+}, O^{1+}	Sum of 3 Gaussians/Kappa-functions	ToF-histogram

Table 3.1: Overview of the ion species, corresponding fit functions, and data product used for the fits.

proved that by running several TRIM simulations in the energy range of helium ions in the solar wind. Thus they can be fitted with a simple 2D-Gaussian. As O^{6+} is a very abundant solar wind heavy ion its peak height is quite high compared to the surrounding peaks. This is why any disturbance by neighboring peaks can be neglected and this peak can also be fitted with a 2D-Gaussian.

The iron series is a sequence of multiple peaks belonging to different charge states. Considering eqn. 2.11 one can easily see that ions with the same mass should lie on a hyperbola in the E-T matrix. In the EpQ-steps considered here these states were Fe^{8+}, Fe^{9+}, Fe^{10+}, Fe^{11+}, and Fe^{12+}. The distances between the peaks are rather small and the abundances of the ions are comparable. Thus it is necessary to fit all five peaks simultanously to find the correct position of a single ion. Consequently, a sum of five 2D-Gaussians was fitted to the iron series. The energy loss in the foil does not necessarily behave like a Gaussian distribution for iron at the considered energies. It would be more precise to assume a distribution similar to that used when considering the energy loss of HPUI (cf. fig. 3.7). Nevertheless, this function is sufficient to find the position of the maxima of the peaks. As the peak heights get smaller when considering the outer peaks of the sequence, only the peaks of Fe^{10+} and Fe^{11+} were used for the calibration, but all 5 peaks were fitted.

The HPUIs have low energies when hitting the carbon foil, which results in an asymmetric energy spectrum after passing the foil. This is due to the fact that ions that loose much energy in the first layers of the foil tend to loose more energy in the remaining layers than ions that do not loose that much energy in the first layers (Lindhard and Scharff, 1961). This effect can be described with a so-called κ-function that forms a tail towards higher ToFs (Köten, 2009). This function was fitted to the "right side" (higher ToF) of the peaks. The "left side" (lower ToF) of the peak can be described by a simple Gaussian function. Thus the complete function reads:

$$f(\tau) = A_0 \cdot \begin{cases} \exp\left(-\frac{(\tau-\tau_0)^2}{2\sigma_l^2}\right) & \text{if } \tau \leq \tau_0 \\ \left(1 - \frac{(\tau-\tau_0)^2}{\kappa_r \sigma_r^2}\right)^{-\kappa_r} & \text{if } \tau > \tau_0 \end{cases} \tag{3.1}$$

with the ToF, τ, the position, τ_0, height, A_0, Gaussian width, σ_l. The additional parameters of the κ-function are σ_r, corresponding to the width of the distriution,

and κ_r, that is a measure for the shaping of the tail. Low κ_r values correspond to a pronounced tail vice versa. In the following this function will be called Gauss-κ-function. The peaks of C^{1+}, N^{1+} and O^{1+} were fitted with a sum of three of these functions. As the N^{1+} peak does not have sufficient statistics for a reasonable fit, its position was approximated by

$$\tau(N^{1+}) = \tau(O^{1+}) - \frac{\tau(O^{1+}) - \tau(C^{1+})}{\sqrt{16} - \sqrt{12}}\sqrt{16}. \qquad (3.2)$$
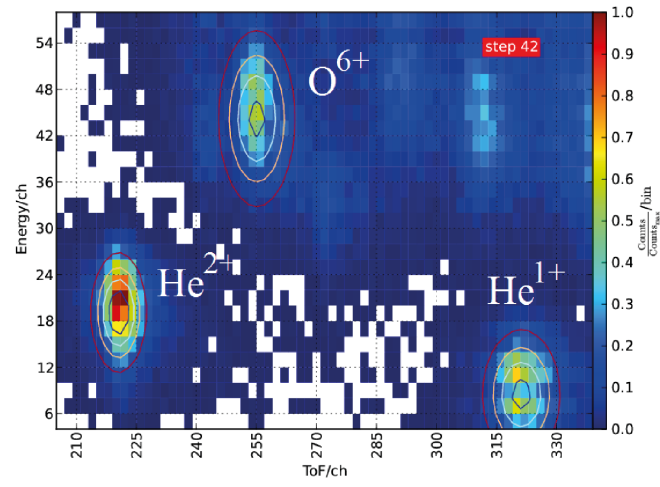
which follows from considering eqn. 2.7 and assuming a constant energy loss α. For σ_l, σ_r, and κ_r the mean values of its neighboring peaks were used and the only free parameter was the peak height A_0. Only with this fit it is possible to determine the most probable ToF position of O^{1+} even though its peak maximum might be shifted by a tail of the other ions.

For a more detailed explanation of the fit procedure the reader is refered to the appendix, where the theoretical background of maximum-likelihood fitting is discussed and the implementation used to perform these fits is given. If not specificly stated, all fits have been performed assuming underlying Gaussian statistics. This results in a so-called least-squares fit (Press, 2007).
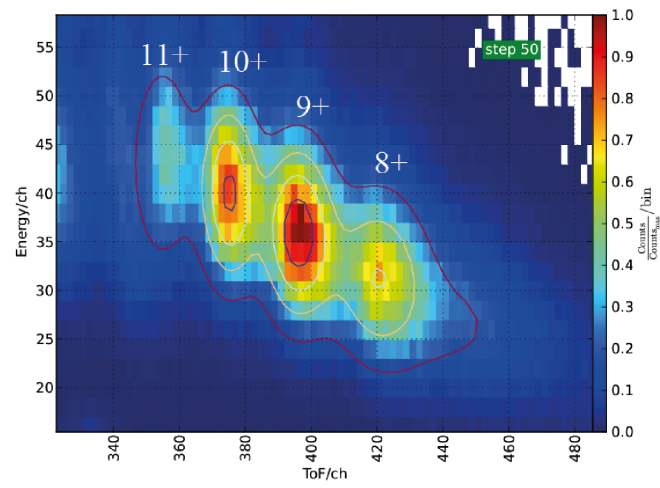
The resulting ToF positions of the ions at various EpQ-steps for DOY 150-230 are displayed in fig. 3.4. The positions form rather smooth curves except for C^{1+} and O^{1+}, where the very low statistics cause a larger variance.

Figure 3.3 *(following page)*: a) Fit of the He^{1+}, He^{2+} and O^{6+} peak at EpQ-step 42 with a 2D-Gaussian. b)Fit of the iron series at EpQ-step 50 with a sum of 5 2D-Gaussians. c)Fit of the C^{1+}, N^{1+} and O^{1+} peaks at EpQ-step 15 with a sum of three Gauss-κ-functions.

a)

O^{6+}

step 42

He^{2+}

He^{1+}

b)

11+ 10+

9+

8+

step 50

c)

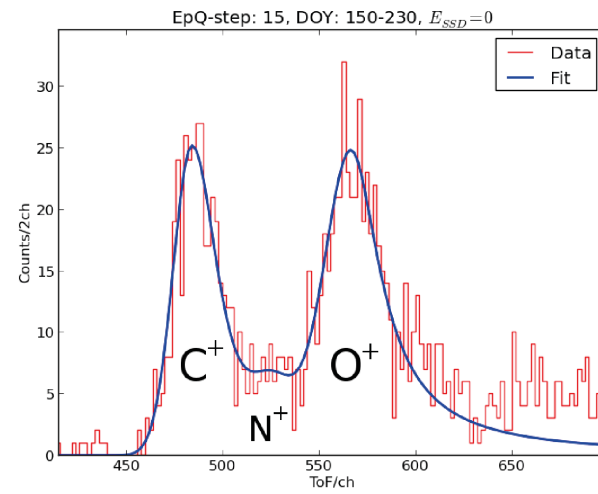EpQ-step: 15, DOY: 150-230, $E_{SSD}=0$
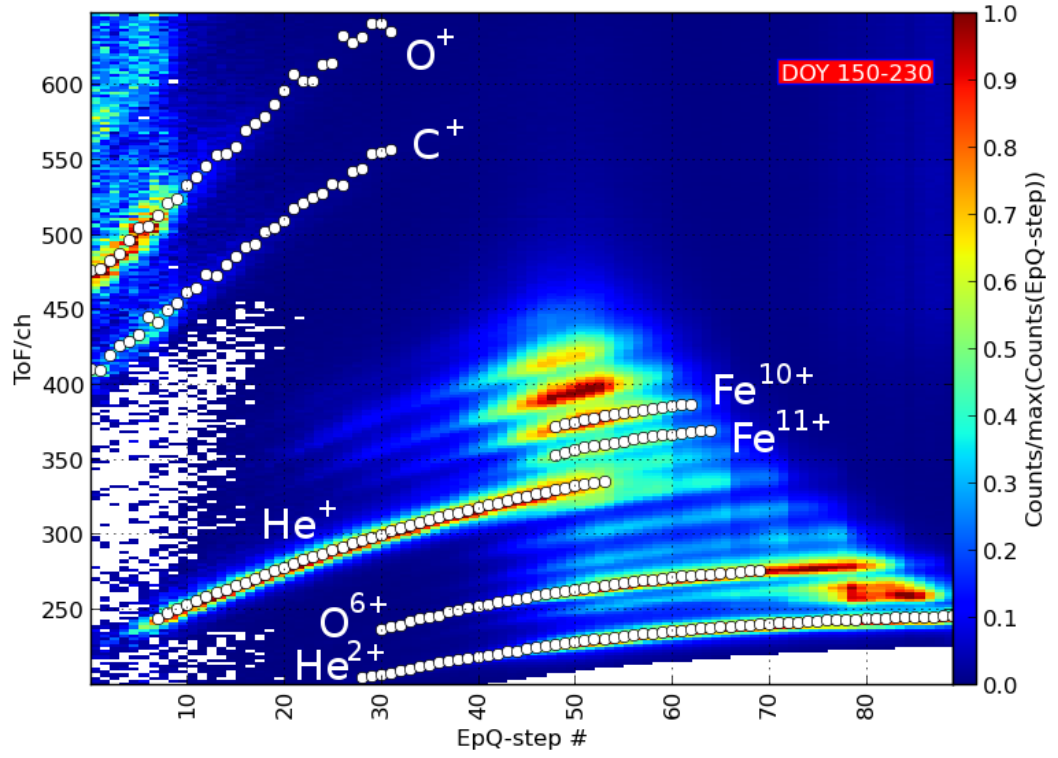
Data
Fit

C$^+$

N$^+$

O$^+$

25

Figure 3.4: 2-dimensional histogram of EpQ-step and ToF. For a better display of the data the color code is normed to the maximum value in each EpQ-step. The white dots indicate the fitted position for the ion species used for the in-flight calibration.

3.2 Modelling the energy loss in the carbon foil

For the calculation of the MpQ from the ToF and EpQ it is necessary to estimate the most probable energy loss of the ions in the carbon foil. This was performed using TRIM simulations. The analytical treatment of the energy loss is rather complicated, because the ions entering the CTOF sensor have energies in the order of $\sim 100\text{keV}$ which is below the validity range of the Bethe-Bloch formula, where only ion-electron interactions are taken into account. At the energy range of CTOF, which lies in the so-called Lindhard-Scharff region of energy deposition (Lindhard and Scharff, 1961), the energy loss of the ions is additionally influenced by atomic recoils and hence the nuclear stopping power of the target cannot be neglected. Consequently the total stopping power of the carbon foil consists of two terms, the electronic and nuclear stopping power (Ziegler et al., 2010):

$$-\frac{dE}{dx} = S(E) = S_e(E) + S_{nuc}(E) \tag{3.3}$$

TRIM calculates these stopping powers independently. Hence the ions loose discrete amounts of energy by nuclear collisions, while the electronic stopping causes a continuous energy loss. The nuclear stopping power for a single ion is calculated by a binary collision approximation. This means that the impact parameter for a single ion-atom collision is randomly chosen and the ion has a constant mean free path between the collisions. For a single collision the Coulomb potentials of the involved particles are reduced to an interatomic potential, which is a screened Coulomb potential. The scattering integral is then solved by an analytical approximation and its result is used to derive the transfered energy. Furthermore statistical algorithms that average over many collisions make the calculation more efficient. The electronic stopping power of heavy ions is calculated according to the energy of the projectile ion, where three cases are distinguished: low-, medium- and high-energy. The energy range covered in CTOF corresponds to the low-energy range of electronic stopping of TRIM, where a velocity proportional stopping power is assumed.

Several TRIM simulations were performed for every element used in sec. 3.1.3 in the energy range of the corresponding EpQ-steps for a foil of 100% carbon with a thickness $d = 200\text{Å}$. Energy histograms were created for the transmitted ions and the most probable energy loss was determined by a fit with an asymetric function similar to eqn. 3.1, but with the κ-tail towards lower energies. In fig. 3.5 an example showing the histogramed energies of transmitted 200keV Fe-ions through 200Å carbon with the corresponding fit is shown.

The found energy losses $\alpha(i, E_{post})$ are then interpolated to estimate the energy loss of the elements at arbitrary energies. TRIM does not discriminate between different charge states of incoming ions, because the original charge state of the ion
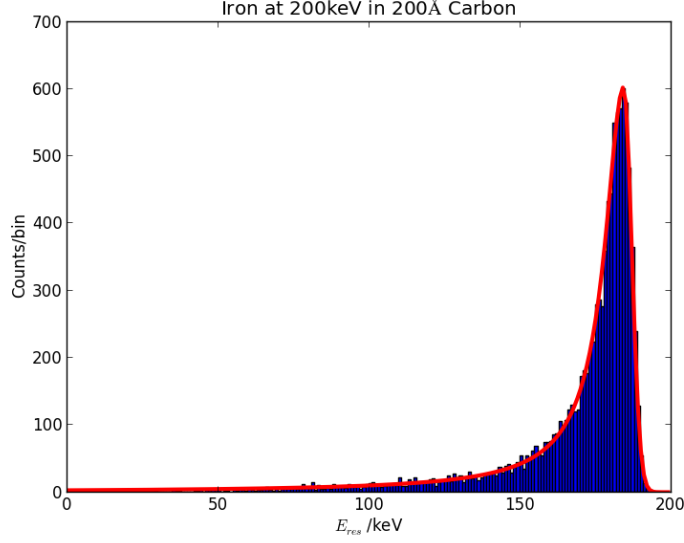
Figure 3.5: Histogram of transmitted energy of 200keV iron ions through a 200Å pure carbon foil. The red line is a fit of an asymmetric κ-/Gaussian-function, that was used to derive the most probable energy loss.

changes right after entering the matter. In its calculations TRIM uses the concept of an effective charge that is dependent on the ion's energy. Therefore there is only one α-curve for helium, carbon and iron, but two curves for oxygen, because the energy range covered for O^{1+} and O^{6+} differs to a great extent and by fitting one curve for each energy range a better accuracy is reached.

The interpolation of the energy loss was done with a fit of the data points with a hyperbola of the following form:

$$\alpha(i, E_{post}) = \frac{p_0}{E_{post} + p_1} + p_2 \qquad (3.4)$$

The hyperbola is not physically motivated, but describes the distribution of the determined α points very well. This can be seen in fig. 3.6, where the α-curves and data points for 200Å foil thickness are shown. As $\alpha = \frac{\Delta E}{E_{post}}$, a hyperbola in α over E_{post} means that the absolute energy loss in the foil, ΔE, is somehow proportional to the energy of the ion before passing the foil E_{post} (cf. eqn. 2.3).

To anticipate to the next section, this procedure was not only performed for a foil thickness of $d = 200$Å, but also for thicknesses of 200Å to 250Å in steps of 10Å. In this manner the parameters p_0, p_1 and p_2 from eqn. 3.4 were determined for all values of d. One can see in fig. 3.7 that the energy loss is rather sensitive to the foil thickness especially at low energies, which complicates the calibration.
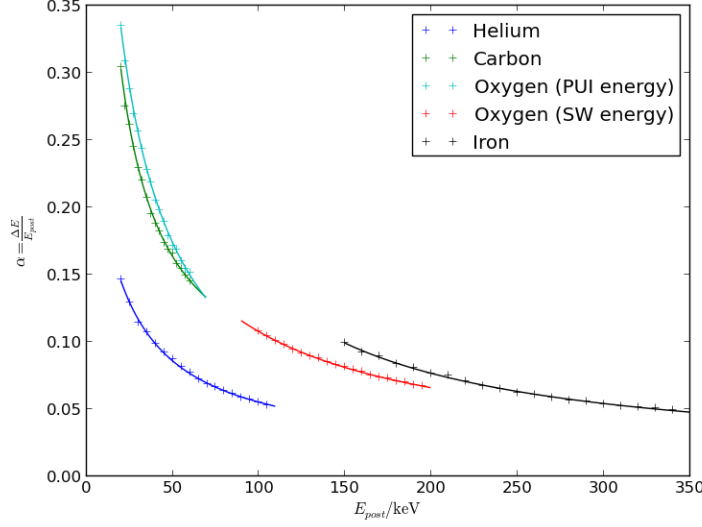
28

Figure 3.6: The symbols display the values for $\alpha = \frac{\Delta E}{E_{post}}$, the ratio of energy loss and impact energy, for He, C, O and Fe. The lines are a hyperbolic fit of the corresponding data points to interpolate α for arbitrary impact energys.

3.3 Optimization of post-acceleration voltage and foil thickness

The last piece of information that is missing to apply eqn. 2.8 to the ToF and EpQ information is a conversion function for the ToF from channels to physical units.

To derive this we can calculate the theoretical ToF (in ns) for the fitted ion peaks at the associated EpQ-steps via eqn. 2.7 and plot it over the position determined by the peak-fit (in ch). For the foil thickness and post-acceleration voltage we assumed the values given in table 2.1. From the area density of the carbon foil a thickness of $d \approx 200\text{Å}$ follows. The result is shown in fig. 3.8. The ADC should be linear in time and hence the data points should form a straight line. But especially when comparing the Fe-ions and the HPUI one can see that there are clear deviations.

The idea is now to optimize the values for the post-acceleration voltage U_p and the foil thickness d as it has been performed for ACE/SWICS by Köten (2009). There it was found that an adjustment of the post-acceleration voltage led to an improved fit of the fitted and the calculated ToF positions of the ion peaks used for calibration.

The other parameter that introduces an uncertainty is the foil thickness d. When
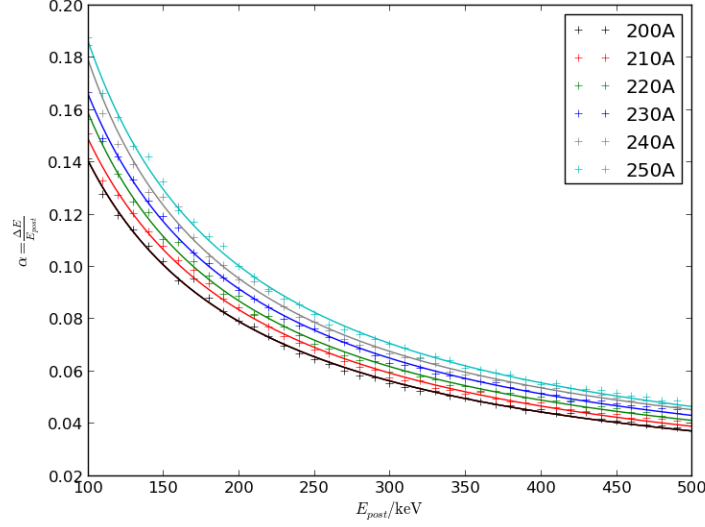
Figure 3.7: Ratio α of energy loss ΔE and impact energy E_{post} for iron ions at carbon foil thicknesses between 200Å and 250Å.

mounting these very thin carbon foils, they suck up water or other ingredients that the solution they swim in contains. This means that the assumption that the foil is made of 100% carbon is not justified and it is very difficult to make assertions about the real thickness of the foil. Furthermore the foil might not be perfectly flat, especially after some time when many fast ions have passed the foil. This may also cause instrumental aging effects that are not considered in this work.

The covalent radius of carbon atoms is ~ 70pm (Holleman et al. (1995)), which means that the bonding length is of the order of a $1 - 2$ Å. When now considering the energy losses simulated in sec. 3.2, especially fig. 3.7, one can see that the most probable energy loss can vary up to a few percent when there is just a variation of some monoatomic layers in the foil thickness. All these effects make it hard to develop a sophisticated model for the energy loss in the carbon foil. Therefore we simply consider carbon foils with different thicknesses to model the energy loss in this work.

Our goal now is to find the values of the post-acceleration voltage and the foil thickness that best describe the fitted ToF positions. For this purpose the theoretical ToF of the ions at a sample of EpQ-steps was calculated for every combination of
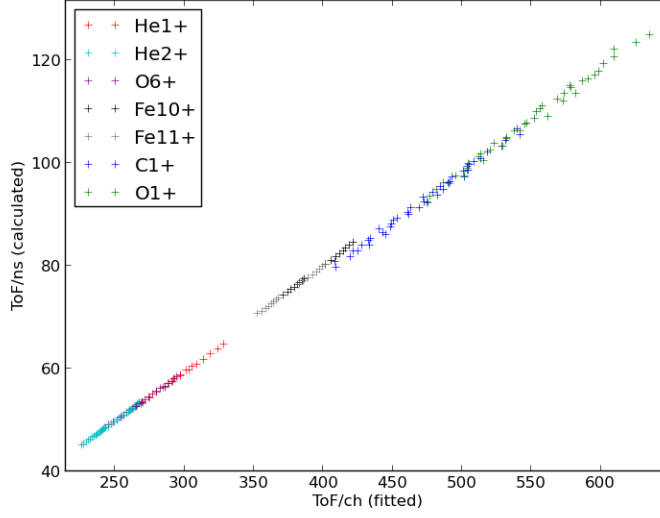
Figure 3.8: Theoretical ToF (in ns) calculated from eqn. 2.7 using the values given in the housekeeping data and $d = 200\text{Å}$ over the fitted ToF values (in ch). With an ADC linear in time the points should form a straight line which is obviously not the case.

d and U_p with

$$
\begin{aligned}
d &\in \left\{ 200\text{Å}, 210\text{Å}, 220\text{Å}...250\text{Å} \right\} \\
U_p &\in \begin{cases} \{18.00kV, 18.01kV, 18.02kV...20.99kV\} & \text{for DOY 82-145,} \\ \{22.00kV, 22.01kV, 22.02kV...24.99kV\} & \text{for DOY 150-230.} \end{cases}
\end{aligned}
$$

The sample of EpQ-steps for every ion is listed in table 3.2. Note that the ToF positions of the HPUIs C^{1+} and O^{1+} were not used in the optimization, because of the low statistics of the peaks in the corresponding ToF-histograms which already resulted in a bigger variance in the EpQ-ToF curve. But these ion species can finally serve as a test whether the MpQ-conversion also works in the MpQ range of HPUI. The other EpQ-steps have been picked according to their peak statistics and background data to ensure a well-fitted ToF position. Furthermore only every second EpQ-step was taken into account to enable a faster calculation. But the number of data points should be still sufficient to derive a working calibration. Then a standard least-square fit of a straight line to the data is performed and the quadratic deviation $\chi^2 = \sum (\tau_{data} - \tau_{fit})^2$ from the data to the fit is calculated. The minimum of χ^2 gives the optimal parameters for our model. In fig. 3.9 a 2D-plot of foil thickness and post-acceleration voltage with the color-coded deviation is plotted for DOY 82-145. The minima of $\chi^2(d, U_p)$ can be found at

31

Ion	EpQ-steps
He^{1+}	17, 19, 21, ... ,33
He^{2+}	48, 50, 52, ... ,80
O^{6+}	36, 38, 40, ... , 58
Fe^{10+}, Fe^{11+}	48, 50, 52, ... ,64

Table 3.2: List of EpQ-steps that were used for the optimization for each ion species involved.

- $d = 240$Å and $U_p = 19.82$kV for DOY 82-145,

- $d = 240$Å and $U_p = 23.85$kV for DOY 150-230.

From the fit of the data points of both time ranges together, one obtains the conversion function between channels and physical units:

$$\tau\,[\text{ns}] = 0.200723 \frac{\text{ns}}{\text{ch}} \cdot \tau\,[\text{ch}] - 1.46909\text{ns} \tag{3.5}$$

In Aellig (1998) a slope of the ADC of $0.19\frac{\text{ns}}{\text{ch}}$ is given, which results in a deviation of $\sim 5\%$ from our findings. The carbon foil of CTOF seems to be 40Å thicker than stated in Aellig (1998), which could be due to the mounting process, where these foils can suck up water. The optimal post-acceleration voltages both show the same trend: In both cases the optimal value lies about 1kV above the value stated in the housekeeping data. Köten (2009) found a similar behaviour for his model of ACE/SWICS.

In fig. 3.10 the theoretical ToF that was calculated with the optimized parameters, is plotted vs. the fitted position. One can see that especially the position of the iron ions have improved compared to the deviation in fig. 3.8. Even the C^{1+} and O^{1+} HPUIs that were not used for the optimization are in good agreement with the fitted line, which is a strong argument for a working calibration.

An important remark is that these values must not be regarded as the "real" properties of the CTOF sensor. As already mentioned, the thickness and composition of the foil is complex and we chose a very simple approach to model the resulting energy loss of passing ions. Furthermore it is rather unlikely that the post-acceleration voltage is indeed 1kV higher than stated in the housekeeping data. These consideration also apply to eqn. 3.5, which may not describe the actual slope and offset of the ADC used in CTOF. Nevertheless the optimized parameters together with eqn. 2.8 or 2.7, respectively, and eqn. 3.5 provide a good description of the data measured in-flight.

A crucial effect that we have neglected until now is the angular scattering of the ions after passing the foil that increases the flight distance and ToF, respectively.
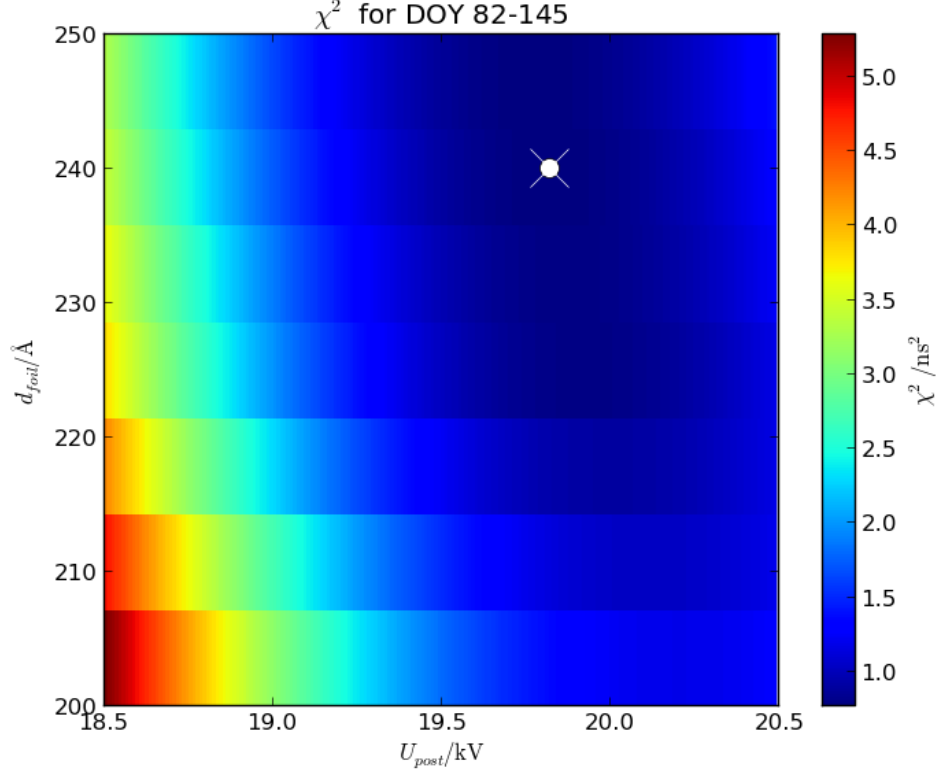
Figure 3.9: For every combination of parameters a fit of theoretical over fitted ToF (see fig. 3.8) with a straight line was perfomed. In this figure the quadratic deviation that is a measure for the goodness of fit is plotted for every parameter combination and the data from DOY 82 to 145. A minimum forms at $d = 240\text{Å}$ and $U_p = 19.82\text{kV}$.

We have neglected this due to the effective area of the SSD given in Hovestadt et al. (1995) of $A = 25\text{mm}^2$, which is probably wrong. With an SSD of this size the enlargement of the ToF distance due to angular scattering would indeed be very small. However, in Aellig (1998) the area of the SSD is stated to be $A = \pi \cdot (25\text{mm})^2$, which means that angular scattering can certainly matter.

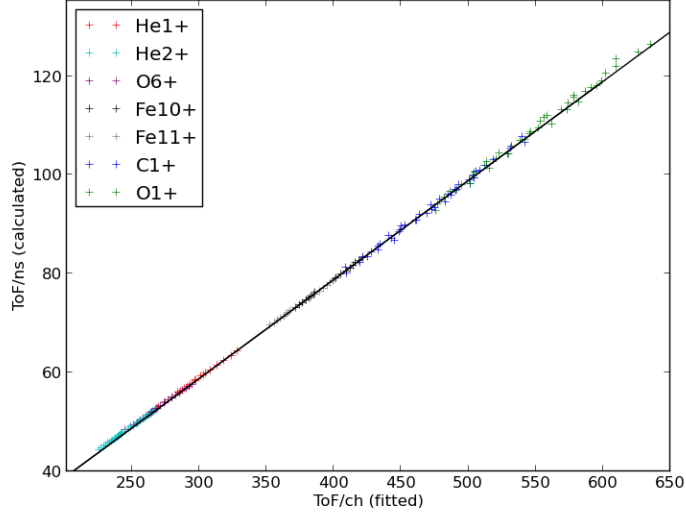Figure 3.10: Theoretical ToF (in ns), calculated with the optimized parameters and eqn. 2.7, vs. fitted ToF (in ch). The black line is a fit to all data points that displays the conversion from ch to ns.

3.4 Results

The resulting conversion function from EpQ and ToF values to MpQ values has to fulfill the following requirements:

The peak position of an ion in an MpQ-spectrum has to:

1. correspond to its MpQ, especially if the actual energy loss of the ion was assumed in the conversion,

2. stay constant for all EpQ-steps,

3. be the same for both time periods.

As the first requirement was the fundamental goal of the calibration, it is somehow trivial and self-fulfilling. But one can easily convince oneself that it is fulfilled by plotting the fitted positions vs. the EpQ-steps and calculating the theoretical ToF in channel numbers for the different MpQ values and energy losses with eqn. 2.7 and 3.5. This is shown in fig. 3.11. For the review of the other requirements only the HPUI peaks are considered, because these ions can clearly be resolved in the MpQ-spectra due to their outstanding high MpQ. Therefore the MpQ-Spectra have been derived on the basis of the energy loss of C^{1+}. Moreover this work's focus lies on the investigation of HPUI justifying this approach.
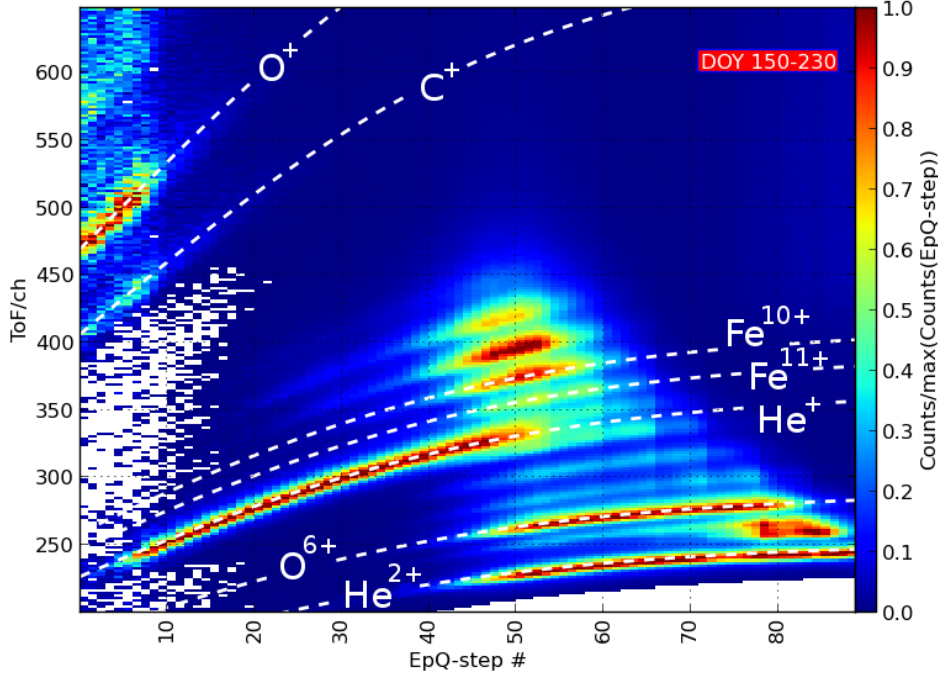
Figure 3.11: The same 2-dimensional histogram of EpQ-step and ToF like fig. 3.4, but now with the predicted ToF positions from the optimized model for the fitted ions. The lines follow clearly the curves suggested by the histogram.

Fig. 3.12 shows a 2D-histogram of the EpQ-step number and the MpQ with the color-coded counts of the events. For a better display of the HPUI peaks a filter for $w_{C^+} \geq 1$ was applied to the data. One can see that the position of the C^{1+}-peak is constantly at $MpQ \approx 12\frac{amu}{e}$ and the O^{1+}-peak is at $MpQ \approx 16.2\frac{amu}{e}$ shifted according to the higher energy loss of oxygen in the carbon foil. Furthermore no significant EpQ-step dependent drifts of the peak positions can be observed. Consequently the second requirement is fulfilled for the HPUI peaks.

Finally, the projection of the counts of fig. 3.12 onto the MpQ-axis is shown in fig. 3.13 for both time periods. It can clearly be seen that the MpQ conversion works in the same way for both time periods, because the peak positions are the same and the peak shapes are comparable. The peaks of the time period DOY 82-145 seem to be a little broader which is caused by the lower post-acceleration voltage within this time period. This means that our third requirement for the conversion function is fulfilled for the HPUI peaks.

Thus all our requirements for a satisfying MpQ-conversion function are fulfilled and the calibration of the ToF information is completed. With eqn. 2.8, the
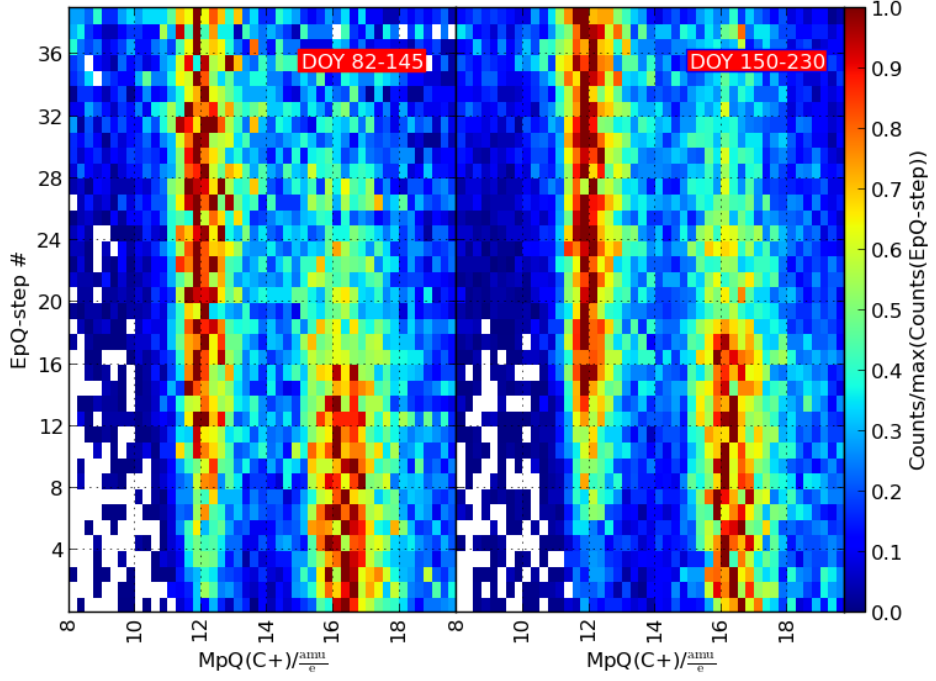
Figure 3.12: 2-dimensional histograms of EpQ-step and calculated MpQ, where the energy loss of C^{1+} was assumed for DOY 82-145 (left-hand-side) and DOY 150-230 (right-hand-side).

energy losses simulated in sec. 3.2, optimized parameters and the channel-to-ns conversion for the ToF from sec. 3.3 a function calculating the MpQ from EpQ and ToF values was found that describes the CTOF data satisfyingly well. The final conversion function reads:

$$\frac{m_i}{q_i} = 2\frac{\tau^2}{l_\tau^2}\left(\frac{E_{kin}}{q_i} + U_p\right)(1 - \alpha(i, E_{post})) \tag{3.6}$$
$$\text{with} \quad \tau\,[\text{ns}] = 0.200723\frac{\text{ns}}{\text{ch}} \cdot \tau\,[\text{ch}] - 1.46909\text{ns}$$
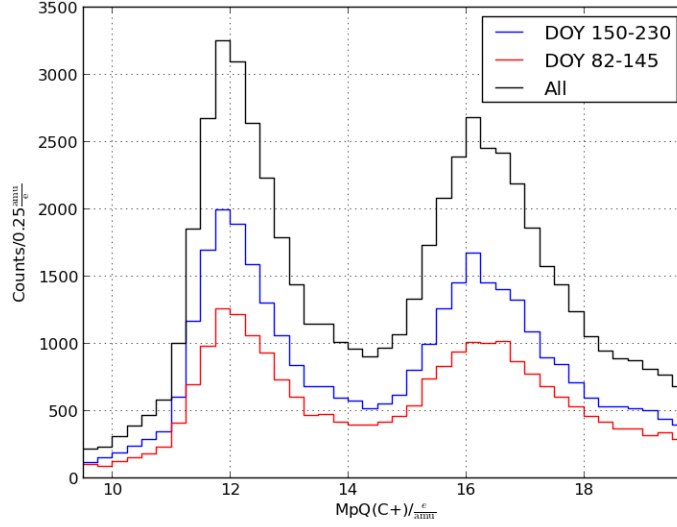
Figure 3.13: Histogram of calculated MpQ values with an assumed $\alpha(C^{1+})$ comparing the result for the different time periods.

The further parameters are:

- $l_\tau = 70.5$mm,

- $U_p = \begin{cases} 19.81\text{kV} & \text{for DOY } 82 - 145, \\ 23.85\text{kv} & \text{for DOY } 150 - 230. \end{cases}$

- $\alpha(i, E_{post})$ calculated from TRIM simulations using a carbon foil with $d = 240\text{Å}$ thickness and

- $\frac{E_{kin}}{q_i}$ calculated from the EpQ-step number with eqn. 2.2.

This conversion function will be applied to the data to study HPUIs in the next chapters. As already mentioned in the beginning of this chapter, the energy loss of one specific ion species has to be assumed when converting EpQ-steps and ToF into MpQ values. Only then the conversion will yield correct results for this ion species. In the analysis, where HPUIs are investigated, always the energy loss of C^{1+} will be assumed. The corresponding MpQ value will be denoted $MpQ(C^{1+})$ to make clear, with which assumed energy loss the value was calculated.

37

Chapter 4

Data Analysis

In this chapter the conversion algorithm from ToF and EpQ-step values into MpQ-values is used to investigate HPUIs. Especially the composition of inner-source HPUI and w-spectra of C^{1+}, O^{1+} and Ne^{1+} are derived.

First a model for the peak shapes is developed to resolve rare HPUIs like Ne^{1+} or Si^{1+} in a fit of MpQ-spectra. Then one special time period is considered, where CTOF measured O^{1+} ions originating from Venus' atmosphere, the so-called Venus tail rays. Due to the relatively high abundance of O^{1+} ions having almost the same energy, this time period serves as an excellent test for our peak shape model.

After this, the relative abundances of the HPUIs are derived for a w-range, where the inner-source contribution is supposed to be dominant over the interstellar contribution. These relative abundances are compared to solar wind elemental abundance ratios. It is widely believed that the inner-source PUIs originate from solar wind ions, that are neutralized due to the interaction with dust particles (e.g. Gloeckler et al. (2000), Wimmer-Schweingruber and Bochsler (2003)). We therefore compute the composition of such a source by multiplying the solar wind elemental abundance ratios with calculated photoionization cross-sections. These results are also compared to our measured inner-source HPUI composition. Finally w-spectra for C^{1+}, O^{1+} and Ne^{1+} are created and analyzed.

4.1 Peak position estimation

First of all, we estimate the position of the ion peaks in a MpQ-histogram, where the energy loss of C^{1+} was assumed. When considering one constant EpQ-step, different HPUIs loose different parts of their energy in the carbon foil. But when converting the EpQ-step and ToF value into MpQ, the energy loss of one specific ion species has to be assumed (cf. sec. 3.4). When considering HPUIs, always the energy loss of C^{1+} was assumed in this work (except for sec. 4.4.3). Only for

the assumed ion species, the MpQ is calculated correctly. The deviation of the MpQ values of the other ion species depends on the difference of the energy loss of this ion compared to the energy loss of the ion species that was used for the calculation. This deviation is now estimated by considering the differences in the energy loss.

For all ions TRIM simulations are performed to deduce their energy loss in the carbon foil, $\alpha(E_{post}, i)$ (see also sec. 3.2). In fig. 4.1 the corresponding curves are shown. All curves show a different behaviour, which means that the difference of the energy losses depends on the energy after post-acceleration. First, the peak positions are estimated at the highest energy after post-acceleration that can occur for HPUIs which is ~ 55keV. Therefore, we performed the position estimation that is now explained in detail for a data subset only containing the EpQ-steps 0 to 10, that correspond to the highest energy for HPUIs.

When estimating the position of a given ion i with MpQ x in a MpQ-histogram, where the energy loss of C^{1+} was assumed, the following steps were performed:

1. From the EpQ-step and the ToF information the MpQ is calculated two times: one time assuming the energy loss of C^{1+}, MpQ(C^{1+}), and the other time assuming the energy loss of ion i, MpQ(i). With a working calibration we expect that the peak position of ion i is calculated correctly with MpQ(i).

2. Now we can filter the data for $x - 0.1 <$ MpQ(i) $<$ x $+ 0.1$, which means that the peak is cutted out at the correct position.

3. Then these counts are converted into MpQ(C^{1+}) values and the mean from these is calculated.

For example, the position of the O^{1+} peak was estimated by calculating MpQ(C^{1+}) and MpQ(O^{1+}) for all events with EpQ-steps between 0 and 10. In a MpQ(O^{1+}) histogram the O^{1+} peak is located at $16\frac{amu}{e}$, where it is expected to be. Due to the bigger energy loss of O^{1+} ions compared to C^{1+} at the same EpQ-step, this peak is shifted in a MpQ(C^{1+}) histogram. Now a slice of the counts around the O^{1+} peak in the MpQ(O^{1+}) histogram are cutted out and converted into MpQ(C^{1+}) values. The mean of these values yields a position of this peak at $16.17\frac{amu}{e}$ in a MpQ(C^{1+}) histogram.

With this procedure the position of the peaks in a MpQ(C^{1+}) histogram is found at the highest possible energy for HPUIs. If we consider arbitrary energies this procedure must not be repeated, but we can derive tendencies for the peak position when going down to lower energies. This is done by just comparing the α-curves in fig. 4.1 to the curve corresponding to carbon. If the difference of the energy loss stays approximately constant, like in the case of nitrogen, the estimated position
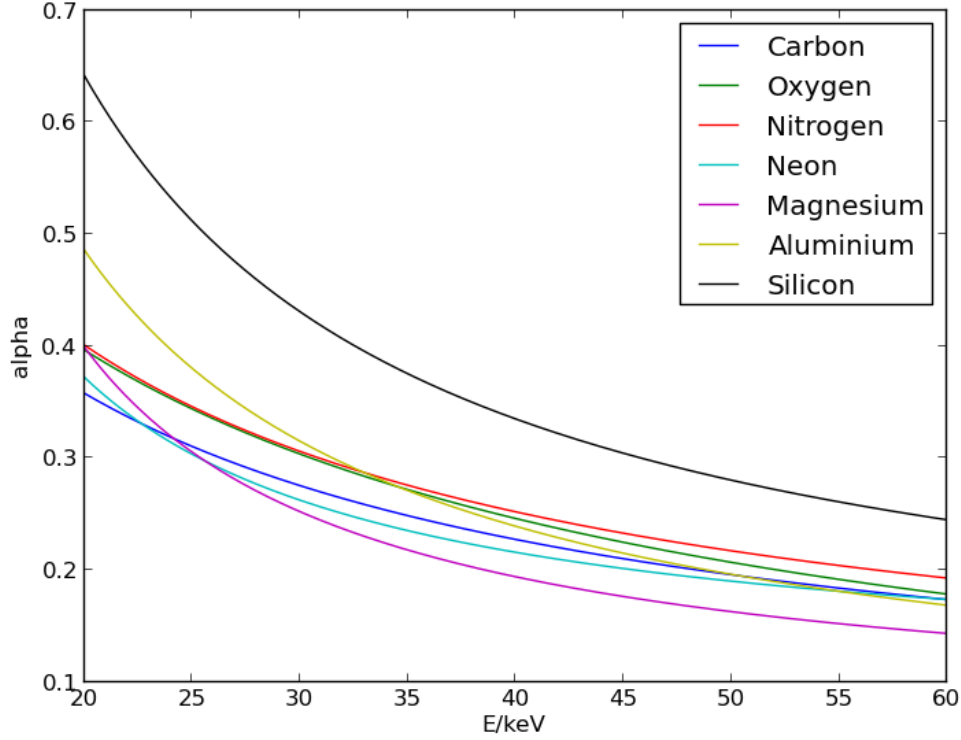
Figure 4.1: Most probable energy loss of ions in CTOF's carbon foil derived from TRIM simulations.

should not change in a different energy range. If the energy loss increases more strongly than the energy loss of carbon when going to lower energies, than the peak position tends to higher MpQ values in a MpQ(C^{1+}) histogram. For example, the difference of the energy loss for oxygen and carbon increases at lower energies. Due to the larger difference, the position of O^{1+} is expected to be at slightly higher values than $16.17\frac{\text{amu}}{e}$ at lower energies than ~ 55keV.
In table 4.1 the findings from this procedure are summarized.

4.2   Prediction of peak shapes

To achieve a reasonable fit of the peaks of rare HPUI like Ne^{1+}, Mg^{1+}, Si^{1+} or even Al^{1+} in the MpQ-spectrum, it is necessary to accurately estimate the corresponding peak shape parameters σ_l, σ_r and κ_r (cf. eqn. 3.1). Then these predicted values may serve as start parameters for the fit or may be used to describe dependencies

Ion	MpQ(C^{1+})-position/$\frac{amu}{e}$	Tendency
C^{1+}	12	$\rightarrow$
N^{1+}	14.36	$\rightarrow$
O^{1+}	16.17	$\uparrow$
Ne^{1+}	20.09	$\downarrow$
Mg^{1+}	23.38	$\uparrow$
Al^{1+}	26.92	$\uparrow$
Si^{1+}	31.13	$\uparrow$

Table 4.1: Summary of ion peak positions in MpQ(C^{1+}) histograms with the position at ~ 55keV and its tendency when considering lower en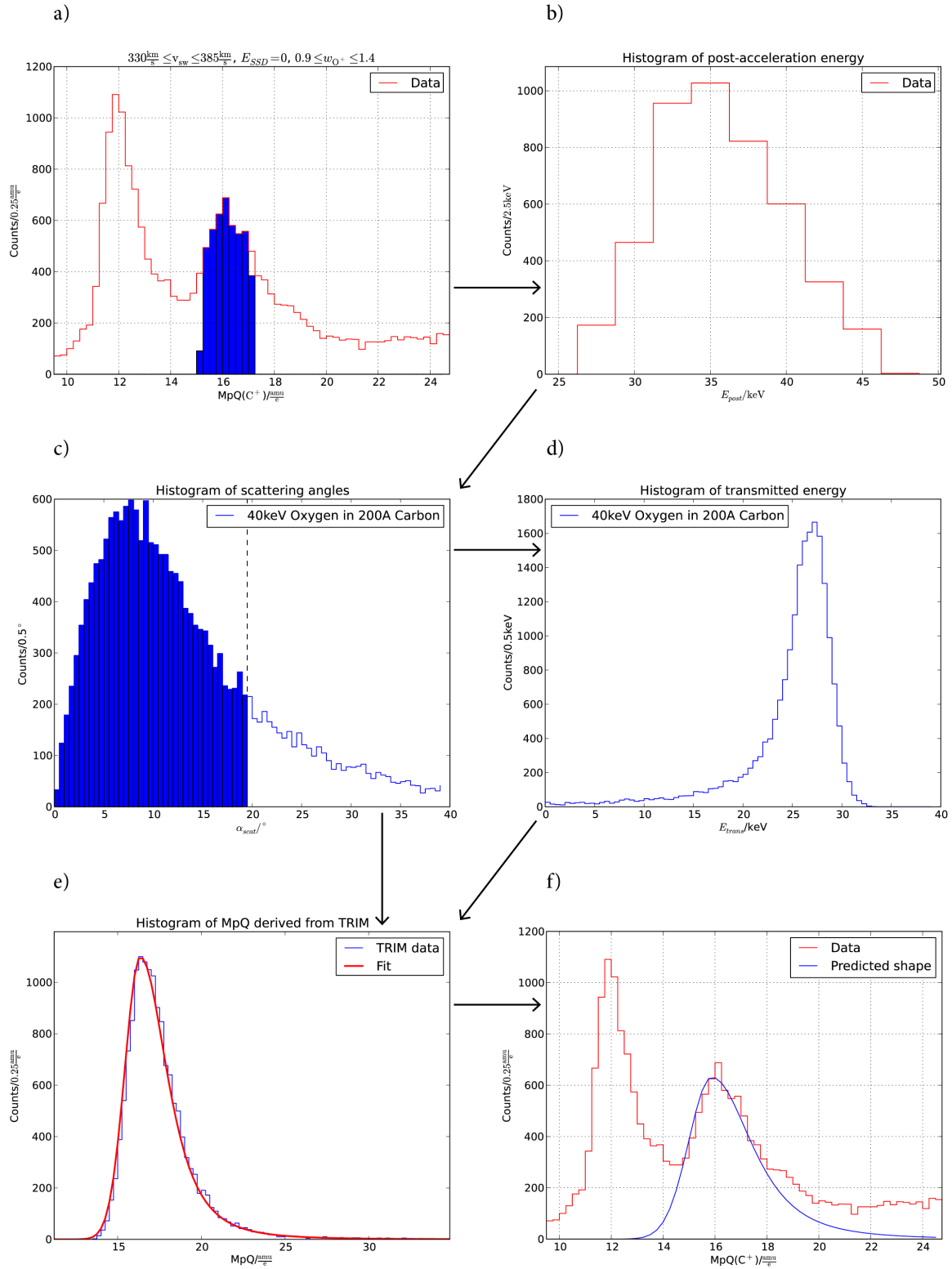ergies. $\rightarrow$: no tendency, $\uparrow$: tendency to higher MpQ values, $\downarrow$: tendency to lower MpQ values.

between the different shape parameters of various peaks. The shape of a peak in a MpQ-spectrum is determined by some instrumental effects. The most dominant ones are the limited bandwidth of the electrostatic deflection system and the statistical energy loss and lateral scattering in the carbon foil that broadens the peaks and causes tail distributions towards larger ToF and MpQ values. Furthermore there might be other effects like non-ideal focusing of the ions or electronic noise that contribute to the peak shapes to a lesser extent. Another non-instrumental issue is that the derived ToF-to-MpQ conversion function might also have an effect on the peak shapes that is hard to quantify.

Especially when considering HPUIs the statistical energy loss and lateral scattering of the ions in the carbon foil gets more and more important. Thus we assume that this is the dominant process that shapes the peaks. As a minimum it gives a good guess for the peak shape parameters. The simulated energy loss and lateral scattering in a carbon foil from TRIM is used to obtain an artificial MpQ-histogram. Then a fit with a Gauss-κ-function is performed to estimate σ_l^*, σ_r^* and κ_r^*.

The detailed procedure for this is now explained on one example peak. Each step is illustrated in fig. 4.2. As example we discuss the O^{1+}-peak in a MpQ-spectrum of the whole data set that has been filtered for $E_{SSD} = 0$, $0.9 \leq w_{O+} \leq 1.4$ and

Figure 4.2 *(following page)*: a) MpQ-histogram of the data filtered for double coincidences, solar wind speed and w_{O+}. The blue shaded bars display the histogrammed counts between $15.2\frac{amu}{e}$ and $17.2\frac{amu}{e}$. b) Histogram of the energy after post-acceleration for the blue counts in a). c)Histogrammed scattering angles from a TRIM simulation of 40keV oxygen ions passing through a 200Å carbon foil. d) Resulting distribution for the transmitted energy for the blue counts in c). e) MpQ-histogram derived from c) and d). Eqn. 3.1 has been fit to the data points (red line). f) Eqn. 3.1 with the same σ_l, σ_r and κ_r fitted via height and position into the original MpQ-histogram a).

a) $330\frac{km}{s} \leq v_{sw} \leq 385\frac{km}{s}$, $E_{SSD}=0$, $0.9 \leq w_{O^+} \leq 1.4$

b) Histogram of post-acceleration energy

c) Histogram of scattering angles

d) Histogram of transmitted energy

e) Histogram of MpQ derived from TRIM

f)

43

$330\frac{\text{km}}{\text{s}} \leq v_{sw} \leq 385\frac{\text{km}}{\text{s}}$. The procedure is the following:

a) In the corresponding figure one can see the MpQ-histogram that serves as example. The peaks of C^{1+} and O^{1+} at $MpQ(C^+) = 12\frac{\text{amu}}{\text{e}}$ and $MpQ(C^+) = 16.2\frac{\text{amu}}{\text{e}}$ can be easily spotted by eye. In this MpQ-histogram the O^{1+} ions are supposed to be between $MpQ(C^+) = 15.2\frac{\text{amu}}{\text{e}}$ and $MpQ(C^+) = 17.2\frac{\text{amu}}{\text{e}}$. All counts in this range were marked with the blue bars in the corresponding figure.

b) As the energy loss and scattering in the foil is energy dependent, the first thing to find out is with which energy most of the ions hit the foil. For this all counts marked in blue in a) are taken to create a histogram of their energy after post-acceleration, E_{post}. The bin containing most of the counts is located at $E_{post} = E_0 = 35$keV.

c) This energy is used to perform a TRIM simulation of oxygen ions passing a carbon foil with $d = 200$Å. The optimized foil thickness from sec. 3.3 was not chosen, because the peak widths that would be reproduced with this foil thickness are too big compared to the peak widths apparent in the data. This could be due to the fact that we neglected angular scattering in the in-flight calibration. Therefore the foil thickness given in Aellig (1998) was chosen. One quantity that is returned by the TRIM simulation is the scattering angle of the ion, that was histogramed in the corresponding figure. One can see that a cut has been drawn at $\gamma = 19.5° = \arctan\left(\frac{r_{SSD}}{l_\tau}\right)$. Ions with larger scattering angles would be lost on the walls of the ToF section and would not be able to trigger a ToF signal.

d) The other quantity used from the TRIM simulation is the transmitted energy of an ion, E_{trans}. In the figure, this quantity was again histogramed showing a reversed Gauss-κ-function.

e) The transmitted energy E_{trans} and the scattering angle γ are combined for every simulated ion to calculate its MpQ value by the following formula:

$$\frac{m}{q} = \frac{2\tau^2}{l_\tau^2} E_0(1 - \alpha(E_0, i))\frac{e}{\text{amu}} \qquad (4.1)$$

with

$$\tau = \frac{\frac{l_\tau}{\cos(\gamma)}}{\sqrt{\frac{2E_{trans}}{m}}}. \qquad (4.2)$$

From this a MpQ histogram is created and the resulting distribution is fitted with a Gauss-κ-function.

f) The fit result provides estimates for σ_l, σ_r and κ_r of the peak in the original MpQ-spectrum. The O^{1+} peak has been fitted with the Gauss-κ-function leaving σ_l, σ_r and κ_r constant on the predicted value. Only the peak position and height were optimized by the fit. One can see that the peak shape is reproduced to a good extent by the predicted parameters.

With this procedure it is possible to predict the peak shape parameters for all considered HPUI at arbitrary energy ranges.

4.2.1 Comparison of model and data

The peak shape prediction procedure explained in the last section is now tested. The peaks of C^{1+} and O^{1+} are used for this purpose. They can usually be seen by eye, which means that one can easily perform a fit with a Gauss-κ-function on these peaks. With such a direct fit of the C^{1+} and O^{1+} peaks the widths of the distributions, σ_l and σ_r, are determined. These widths can then be compared to the predicted values from the procedure explained in sec. 4.2. Unfortunately the tails of the peaks are superimposed by counts of N^{1+} and Ne^{1+}, respectively, and thus no explicit statement about the accuracy of the estimated κ can be made. The fits to determine σ_l and σ_r have been performed in a data subset fullfilling the following conditions:

- $E_{SSD} = 0$

- $330 \frac{\text{km}}{\text{s}} \leq v_{sw} \leq 385 \frac{\text{km}}{\text{s}}$

The v_{sw} range is chosen to limit the energy distribution of the ions and to guarantee sufficient statistics, because in this speed range most of the double coincidences have been measured.
This data subset is then filtered for w_{C+} ranges with $\Delta w_{C+} = 0.1$ from 1 to 1.7 that correspond to different energy ranges. This means that the first $MpQ(C^{1+})$ histogram that was used for the fit was filtered for $1 \leq w_{C+} \leq 1.1$ and so on.
The peaks of C^{1+}, N^{1+} and O^{1+} were then fitted in the histogram using again a sum of three Gauss-κ-functions. Not all parameters of this function were optimized. As the N^{1+} peak is hidden between the C^{1+} and O^{1+} peaks, we used the constant predicted peak shape parameters σ_l^*, σ_r^* and κ_r^* for the calculation of this distribution. Only the position and the height of this peak were optimized. It was mentioned before that we cannot compare the κ_r parameters of the direct fit with the predicted value κ_r^*. Therefore we set $\kappa_r = \kappa_r^*$ for the C^{1+} and O^{1+} peaks and did not optimize this parameter. This means that the remaining free parameters of the C^{1+} and O^{1+} distribution are the position, the height and the two widths, σ_l and σ_r.

The MpQ(C^{1+}) histograms were always created 4 times for one data subset using different bin widths to avoid any effects that could be caused by the binning. The used bin widths are ΔMpQ(C^{1+}) $= 0.2\frac{\mathrm{amu}}{\mathrm{e}}$, $0.25\frac{\mathrm{amu}}{e}$, $0.3\frac{\mathrm{amu}}{e}$ and $0.4\frac{\mathrm{amu}}{e}$. In each of these histograms the fit of the peaks was performed.

In fig. 4.3 the results for σ_l and σ_r for C^{1+} and O^{1+} are plotted vs. the σ_l^* and σ_r^* values predicted by the procedure described in sec. 4.2. First of all, a clear correlation can be observed. The calculation of the correlation coefficient yielded $\rho = 0.97$ confirming the first impression. A least-squares fit of the data with a simple linear function $f(x) = m \cdot x$ was perfomed with $m = 0.96$ as result. Consequently, it is
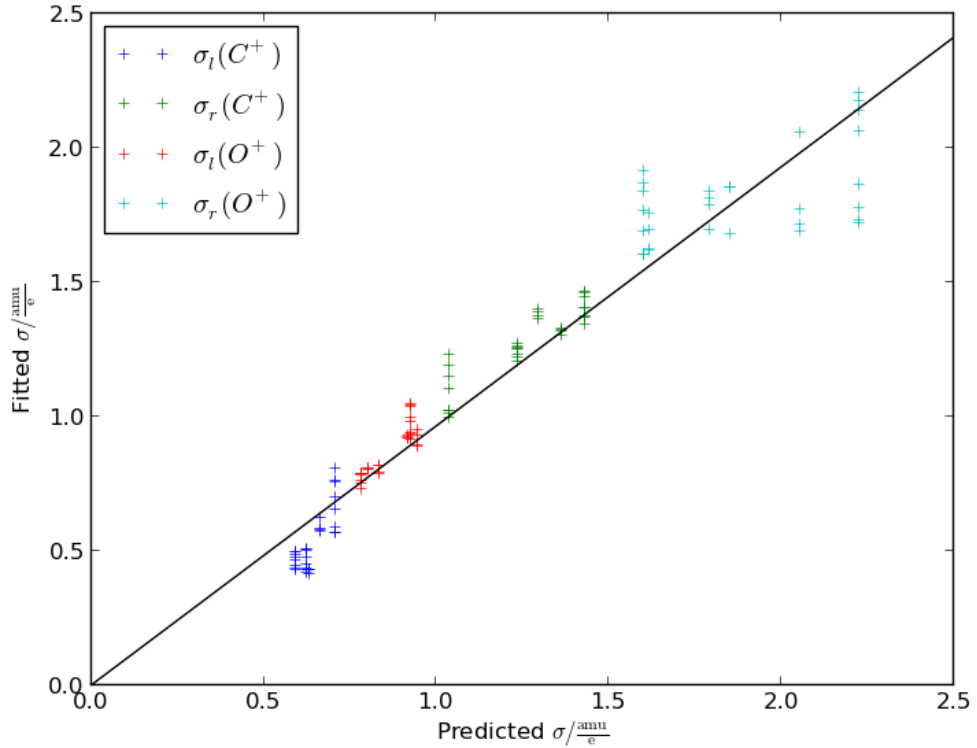
Figure 4.3: Fitted σ values over predicted σ values for w-ranges of $\Delta w = 0.1$ from 1 to 1.7 for C^{1+} with the data filtered for double coincidences and $330\frac{\mathrm{km}}{\mathrm{s}} \leq v_{sw} \leq 385\frac{\mathrm{km}}{\mathrm{s}}$. The black line displays a linear fit of the data points.

found that the peaks seem to be a little thinner than predicted from the energy loss and scattering in the foil. One explanation for this could be that TRIM only approximates the interaction of the ions with the foil with a limited uncertainty. Thus, the results from the TRIM simulations for the width of the transmitted energy distribution might be imprecise.

46

Although it is nearly negligible, because the predicted values will only serve as start parameters for the fits, the correction factor of $m = 0.96$ is applied to the estimated σ^* values to ensure an optimal prediction of peak shape parameters.

4.3 Venus tail rays

Another opportunity to test our calibration and the estimated peak shapes are the so-called Venus tail rays that were observed with CTOF on DOY 165 and 166, 1995 (Grünwaldt et al., 1997). In this time period SOHO was in a close conjunction to Venus and an unusual high amount of O^{1+} ions was measured in three 5-minute cycles. In fig. 4.4 O^{1+} box rates (counts with $15.2\frac{amu}{e} \leq MpQ(C^{1+}) \leq 17.2\frac{amu}{e}$) are shown for every instrumental cycle in the time range of interest. It is commonly assumed that during these three cycles SOHO stayed inside a flux tube carrying ions from Venus' ionosphere. These Venus tail rays have already been investigated by Grünwaldt et al. (1997), where further information about this issue can be found.
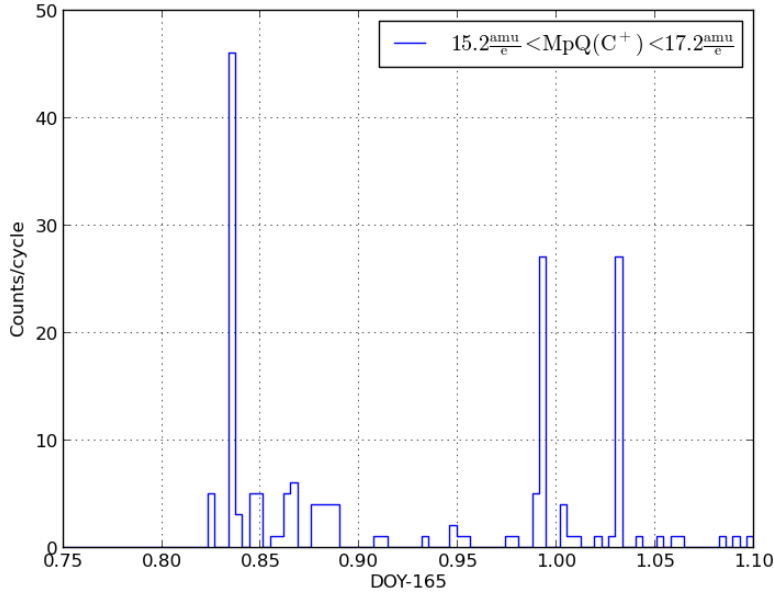

Figure 4.4: Box rates of O^{1+} ions binned in 5-minute cycles. The three cycles with an extraordinarily high amount of O^{1+} counts caused by Venus tail rays are clearly visible.

For us these three cycles are of interest, because they provide a nearly undisturbed

O^{1+} peak in a small energy range that can be used for comparison with our model. Therefore a MpQ-spectrum of these cycles with a binning of $\Delta MpQ_{bin} = 0.5\frac{amu}{e}$ was created that can be seen in fig. 4.5, where ions having $w_{He^{2+}} \geq 2$ have been filtered out to avoid background caused by He^{2+} pile-ups (cf. sec. 4.4.2). Then the procedure described in 4.2 is applied to the spectrum to predict the
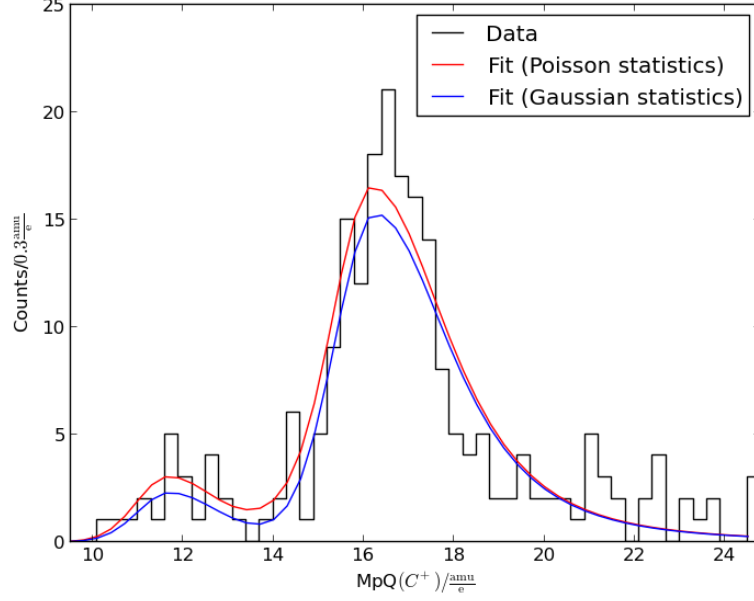

Figure 4.5: MpQ spectrum of the three cycles that can be accounted to Venus tail ray observation. A fit of the position and height of the C^{1+} and O^{1+} peaks have been performed with the model estimation of σ_l, σ_r and κ.

shape parameters of the C^{1+} and O^{1+} peaks. The position and height of the corresponding Gauss-κ-functions (eqn. 3.1) is fitted to the data leaving σ_l, σ_r and κ_r constant for each peak. In one fit procedure Poisson statistics are applied to account for the low count rates (see appendix A), but also a fit using Gaussian statistics is performed. Even though the deviation seems to be quite high by eye, the low statistics have to be considered. A $\chi^2 = 1.07$ for the fit using Gaussian statistics is a measure for the goodness of fit stating a good match of the function and the data. Furthermore, there might also be occasional counts of Ne^{1+} or Mg^{1+} in the tail of the O^{1+} peak that are not considered in the fit. As the estimated shape parameters shall only serve as start parameters for subsequent fits, this goodness of fit is sufficient.

The following investigations focus on the undisturbed solar wind. Therefore, these three cycles treated in this section are excluded from further analysis.

4.4 Inner-source HPUI composition

With the MpQ conversion and the peak shape known, the composition of inner-source PUIs as measured with CTOF can now be estimated. For this we derive the count rates of the different ion species in certain w- and v_{sw}-ranges by a fit of the corresponding MpQ histograms.

For this we have to subtract the background of the MpQ histograms. The peak shape models are used to fit the distributions of all ions to the data. By integrating such a distribution, the count rate for one ion species is calculated. Then the ratio of different count rates is considered to estimate the inner-source PUI composition. This composition is then compared to solar wind composition values and ionization rates.

4.4.1 Fit procedure

We assume that every ion species creates a distribution with the shape of a Gauss-κ-function in a MpQ-histogram of our data. We consider the distributions of C^{1+}, N^{1+}, O^{1+}, Ne^{1+}, Mg^{1+}, Al^{1+}, and Si^{1+}. The challenge is now to fit all distributions at once to the data. If we would fit every single parameter of each function the fit would have to optimize 35 parameters at once, five per ion. On the one hand many optimization algorithms do not cope with that many parameters and on the other hand it is very likely that the fit yields unphysical results. Therefore, we make use of the peak shape models to reduce the number of free parameters. Furthermore boundaries were set to the remaining free parameters to avoid unphysical results. Additionally, a special scheme in the fit procedure is applied to increase the probability that a global deviation minimum is found by the algorithm. These single steps are now explained in more detail:

Reduction of free parameters

For every ion the peak height A, position x_0, the widths σ_l and σ_r, and the parameter κ_r from the Gauss-κ-function (eqn. 3.1) have to be determined. For 7 different ion species, this leaves us with 35 parameters. But we have also 21 parameter estimates from the peak shape model of sec. 4.2 for each of the 7 ions: σ_l^*, σ_r^* and κ_r^*.

First, we set $\kappa_r = \kappa_r^*$ for each ion and leave this parameter constant in the fit. Fur-

thermore we relate the σ_l and σ_r values of the ions among themselves by setting

$$\frac{\sigma_{l,i}}{\sigma_{l,j}} = \frac{\sigma_{l,i}^*}{\sigma_{l,j}^*} \tag{4.3}$$

$$\frac{\sigma_{r,i}}{\sigma_{r,j}} = \frac{\sigma_{r,i}^*}{\sigma_{r,j}^*} \tag{4.4}$$

This has the purpose that the relation of the peak widths always stays constant. It avoids that for example the Mg^{1+} peak is very thin, while the Ne^{1+} peak is very brought after the fitting of the histogram. This would be an unphysical result. By setting these ratios the fit has to adapt all peak widths simultanously. Going back to the example this would mean that if the fit algorithms wants to increase the left width of the Ne^{1+} peak, it must also increase the left width of the Mg^{1+} peak. For the linking we split the ion species into two groups: the C^{1+}, N^{1+}, O^{1+} group and the other ions Ne^{1+}, Mg^{1+}, Al^{1+} and Si^{1+}. As we already tested the predicted peak shapes for C^{1+} and O^{1+}, we link the widths of the first three ions. But we do not know how accurate the peak shapes are predicted for the latter ions. Therefore we link the widths of this group, because we assume that at least all widths behave in the same way compared to the predicted widths.

For each of these groups ratios are calculated, which means that we fit all σ_l and σ_r parameters by optimizing overall 4 parameters. Now we have reduced the number of free parameters from 35 to 18. These are the 7 peak positions, 7 peak heights and the 2 pairs of σ_l and σ_r for the peak widths.

Setting boundaries

To avoid unphysical fit results we set constraints to the fit parameters. Of course every peak height has to be greater or equal to zero. Boundaries for the peak positions were set to ensure that the peaks are fitted where we would expect them to be. For the width parameters, σ, we only allow variations up to 25% from the estimated value.

Fitting scheme

When performing the fit not all paramters are varied together, but only two parameters are optimized at once. A special scheme is chosen to support that the fit algorithm runs into a global minimum:

1. One can show that when always varying the same two parameters together, it is more probable that the fit finds a local minimum (Heidrich-Meißner,

personal communication Nov. 2013). Consequently the parameters that are varied are always chosen randomly in each optimization step. Then these parameters are not varied until every other parameter has been varied once.

2. After every parameter has been varied the reduced χ^2 of the fit result is calculated. If the deviation of the reduced χ^2 from the value of the last fitting round is smaller than 10^{-8} the fit is finished and the result can be displayed.

3. If the deviation is larger than 10^{-8} the procedure starts again with randomly picking two of the free parameters.

An exception from this procedure is made when determining the count rates of C^{1+} and N^{1+}. Usually the count rates of PUI heavier than neon are so small when fitting C^{1+} and N^{1+} that only the peaks of C^{1+}, N^{1+} and O^{1+} are considered and the peaks of the heavier PUI are neglected. As we then have a significantly smaller number of free parameters, the widths of C^{1+} are fitted independently to gain a more precise result.

Sodium and isotopes

Furthermore it has to be mentioned that the distributions of Na^{1+} and the isotopes $^{22}Ne^{1+}$, $^{25}Mg^{1+}$ and $^{26}Mg^{1+}$ are taken into account in the fit, but their parameters are not varied. The ratio of abundances in the solar corona of sodium and magnesium is $\frac{Na}{Mg} \approx 0.05$ (Aschwanden, 2005). Therefore the peak of Na^{1+} ions is considered in the fit function with a height of $A_{Na} = 0.05 A_{Mg}$ and the constant predicted shape parameters derived following sec. 4.2.
The neon and magnesium isotopes are treated similarly, but the peak shape parameters are always taken from the most abundant isotope. The abundance ratios of these are (Wiens et al., 2004):

- $\frac{^{22}Ne}{^{20}Ne} \approx 0.07$,

- $\frac{^{25}Mg}{^{24}Mg} \approx 0.14$ and

- $\frac{^{26}Mg}{^{24}Mg} \approx 0.15$.

No parameter of the corresponding distribution in the MpQ histogram is optimized in the fit. But they are taken into account by distributions with the height $A_{^{22}Ne} = 0.07 A_{Ne}$, $A_{^{25}Mg} = 0.14 A_{Mg}$ and $A_{^{26}Mg} = 0.15 A_{Mg}$. The isotopic composition is expected to be the same for the solar wind as well as for interplanetary dust particles which justifies this approach (Wimmer-Schweingruber et al., 1998). For

the ^{22}Ne^{1+} distribution the σ_l, σ_r and κ_r of ^{20}Ne^{1+} is used. The ^{25}Mg^{1+} and ^{26}Mg^{1+} distributions have the same peak shape parameters as the ^{24}Mg^{1+} distribution. Although the peak widths are expected to get broader with increasing mass, this approximation is sufficient. The isotope peaks are that small that they barely contribute to the total fit.

4.4.2 Background suppression and subtraction

Especially when considering low PUI energies background caused by He^{1+} pile up or iron counts becomes important. By pile up we mean that a He^{1+} ion triggers the START signal at the carbon foil, but does not trigger a STOP signal. The STOP signal is then triggered by the next ion, which increases the ToF and the calculated MpQ, of course. This effect can happen during high fluxes and is hence only relevant for very abundant particles like hydrogen or helium ions. Going to very low PUI energies the tails of the Fe^{8+} and Fe^{7+} (or even lower charge states) ions are superimposed on the counts of the HPUI. Even though the MpQ values of these ions are out of the MpQ range of HPUIs, the tails of the distributions can reach into this MpQ range. The energy loss of iron in the foil leaves a similar signature in the MpQ values as HPUIs (cf. sec. 3.2) causing these tails.

This background has to be subtracted to get a precise result of the HPUI count rates at these energies. But first the background is investigated in more detail. In fig. 4.6 five MpQ-histograms are shown that were created for different energy ranges in a solar wind speed range of $300\frac{\text{km}}{\text{s}} \leq v_{sw} \leq 400\frac{\text{km}}{\text{s}}$. The black and the red curve in fig. 4.6 were created in a range of $0.7 \leq w_{\text{C+}} \leq 0.8$. This corresponds to $1.2 \lesssim w_{\text{He+}} \lesssim 1.4$ and $0.9 \lesssim w_{\text{Fe}^{8+}} \lesssim 1.05$, which means that a large part of the He^{1+} and the Fe^{8+} velocity distribution contributes to MpQ histogram. This again means that due to the He^{1+} pile up and the tails of the iron distributions a big background can be observed. The iron ions are expected to trigger an energy measurement in the SSD due to their high charge. Therefore one can reduce this background caused by iron by only considering double coincidences ($E_{SSD} = 0$). But due to the limited efficiency of the SSD and possibly angular scattering, some of the iron ions do not leave a signal in the SSD. This is illustrated with the red curve.

When going to slightly higher energies, a smaller part of the He^{1+} and the iron velocity spectra contributes to the MpQ histogram. This again reduces the background to a good extent which is shown with the blue curve. Going to even higher energies, as shown with the green curve, one can already neglect the iron contribution to the background. But the very abundant He^{1+} counts still have to be considered. Only at very high energies like $0.9 \leq w_{\text{Mg+}} \leq 1$ (brown curve), which corresponds to $1.3 \lesssim w_{\text{C+}} \lesssim 1.4$ and $2.2 \lesssim w_{\text{He+}} \lesssim 2.45$ the background is almost completely suppressed and can be neglected in the fits of the HPUI distributions.
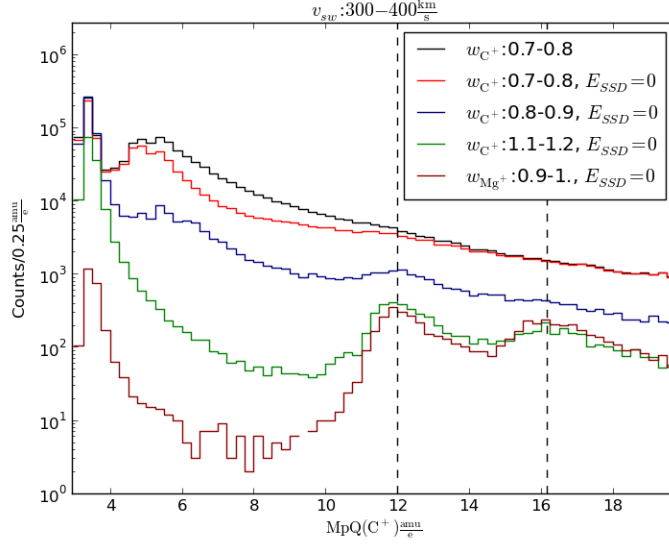
Figure 4.6: MpQ histograms in the solar wind speed range of $300\frac{\text{km}}{\text{s}} \leq v_{sw} \leq 400\frac{\text{km}}{\text{s}}$ to illustrate the influence of the background. Five different energy ranges were used to show how the background is suppressed at higher energies. The peak positions of C^{1+} and O^{1+} are illustrated with dashed lines.

The background subtraction is performed with the help of the fit of the interfering tails. If the background is only caused by the He^{1+} pile up tail like it is the case for the green curve, a κ-function is fitted to the He^{1+} tail. If the tails of iron ions cannot be neglected like it is the case with the blue curve, a Gaussian-κ-function is added, that describes the influence of the iron counts. In cases of very big background (for example the red curve in fig. 4.6), the background treatment is complicated due to many contributions from different ions. In that case only one κ-function is fit in the vicinity of the MpQ range of HPUI to extrapolate the background counts.

4.4.3 Traces of Fe^{3+}

Another effect that introduces background to our measurements is that there are probably counts in the MpQ histograms that are falsely assigned to other ion species. For example the Ne^{1+} count rate could be superimposed by Ca^{2+} counts, because these two ion species have the same MpQ and we cannot distinguish between these ions from our measurement data. Another example for this could be the presence of Fe^{3+} that is investigated in this section.

Iron is an abundant solar wind element that has a quite low FIP (7.9eV[1]). Thus iron PUI should exist according to the production scenarios for which the solar wind is the source for PUI and also in which grains are sputtered or destroyed. Unfortunately Fe^{1+} ions cannot be observed with CTOF. On the one hand only a small amount of EpQ-steps covers the corresponding velocity range, which limits the statistics, and the maximum speed of an Fe^{1+} ion entering CTOF is $v_{max}(Fe^{1+}) = 345 \frac{km}{s}$. On the other hand iron is very heavy and interacts strongly with CTOF's carbon foil. This means that the ToF distribution is very broad and smeared out, if the ions can even pass through the foil.

In contrast to Fe^{1+} the higher charged ions Fe^{2+} and Fe^{3+} lie in the detection range of the sensor. The iron PUIs may exist in these charge states, because the low FIP makes a second or third ionization more likely than for elements with a higher FIP like carbon, nitrogen or oxygen.

A double charged ion gains twice the energy of the post-acceleration voltage of the instrument. Consequently one would expect Fe^{2+} ions to leave a signature in the triple coincidence data. This is not the case. But this does not mean that we can exclude that Fe^{2+} ions have been measured with CTOF and are apparent in the data. We suppose that on the one hand the energy gained by the post-acceleration voltage might not be sufficient for the ions to hit the active area of the SSD due to angular scattering and on the other hand, correlated with this effect, that the distribution in a MpQ spectrum could be too broad to leave a visible signature. We again performed TRIM simulations to investigate this and found that the distribution of the transmitted energies for Fe^{2+} is much broader than the corresponding distribution for HPUIs. This means that the Fe^{2+} counts are smeared out over a large MpQ range and no visible signature can be formed.

The arguments above do not hold for Fe^{3+}. But another problem arises when considering Fe^{3+}: With MpQ(Fe^{3+})= $18.67 \frac{amu}{e}$ and the relative energy loss, α, of Fe^{3+} always being smaller than the relative energy loss of O^{1+} for each EpQ-step the position of the Fe^{3+} signature lies very close to the dominant O^{1+} peak (cf. sec. 4.1). The challenge is now to separate the O^{1+} distribution from the Fe^{3+} counts.

For this a filter for $0.9 \leq w_{Fe^{3+}} \leq 1.1$ and $10\text{ch} < E_{SSD} \leq 30\text{ch}$ is applied to the data to decrease the counts of O^{1+} that would superimpose the rare Fe^{3+} counts. This E_{SSD} range is chosen, because O^{1+} ions have a very low probability for triggering such a high SSD measurement.

Furthermore $\alpha(E_{post}, Fe^{3+})$ is determined to enable the calculation of MpQ(Fe^{3+}) for every count. The peak positions for C^{1+} and O^{1+} in the MpQ(Fe^{3+}) histogram can be calculated analogously to sec. 4.1. Then a MpQ(Fe^{3+})-histogram with ΔMpQ = $0.2\frac{amu}{e}$ is created and a 3-bin running average is performed. The result

---

[1]Taken from `www.nist.gov/pml/data/ion_energy.cfm`

can be seen in fig. 4.7. The estimated positions for C^{1+} and O^{1+} are also illustrated in the figure.

Especially in the 3-bin running average a hump in the tail of the O^{1+} peak directly at MpQ$\approx 18.67\frac{amu}{e}$ can be observed indicating the presence of Fe^{3+} ions in the data. Due to the lack of measurements of Fe^{2+} and Fe^{1+} quantitative evaluations are pointless, because only count rate ratios are reasonable to consider. Furthermore the statistics are very low and the hump itself consists of about 20 counts. On the one hand this means that it could be created by statistic count rate fluctuations, but on the other hand it appears to be directly were the Fe^{3+} peak is supposed to be, although the predicted peak position for O^{1+} is very close. But nevertheless fig. 4.7 marks the first hints towards a direct observation of Fe^{3+} in the solar wind.
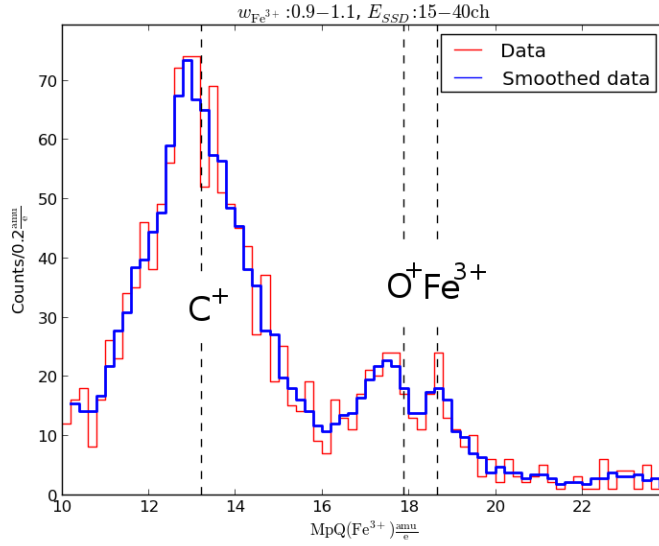
Figure 4.7: MpQ-histogram for counts within $10 < E_{SSD} \leq 30$ch and $w_{Fe^{3+}}$ between 0.9 and 1.1. A 3-bin running average has been calculated (blue line) and the expected peak positions of C^{1+}, O^{1+} and Fe^{3+} are illustrated.

4.4.4 Results

The fit procedure described above can be applied to any MpQ-spectrum to derive the count rates of the different ion species. It is now used to estimate the inner-source PUI composition.

In general, this means that the count rates of HPUIs in a certain w-ranges are determined. By taking the same w-range for the HPUIs, we always compare the

same parts of the velocity distribution to each other. As we expect that all inner-source HPUIs have the same source, the shape of the velocity distribution should also be the same. Furthermore, we do not correct the count rates for the velocity-space volume covered by the sensor, because the count rates are always derived for similar velocities.

The energy coverage of CTOF is limited. For example the maximum velocity of a Si^{1+} ion that can enter the sensor is $v_{max}(\mathrm{Si}^{1+}) = 487\frac{\mathrm{km}}{\mathrm{s}}$. If we want to determine the count rate in a certain range of w values, boundaries are set to the solar wind speeds for which the composition can be measured. For example, if the count rate for Si^{1+} in the w-range of $0.9 \leq w \leq 1.4$ is determined, we can only use the solar wind speed up to $\frac{v_{max}(\mathrm{Si}^1)}{1.4} = 348\frac{\mathrm{km}}{\mathrm{s}}$, because at higher solar wind speeds the sensor does not cover the whole w-range. This is necessary to compare the count rates to each other.

The inner-source PUI component dominates over the interstellar component up to $w \approx 1.4$ (Berger et al., 2013). Therefore the first approach is to derive the count rate ratios in a w-range between 0.9 and 1.4. The lower boundary was chosen, because at $w = 0.9$ the background is still suppressed to a good extent (cf. sec. 4.4.2). The solar wind speed was limited to $v_{sw} < 348\frac{\mathrm{km}}{\mathrm{s}}$ due to the reasons named above.

The count rate of ion i is then determined with the following procedure:

1. The data is filtered for $v_{sw} < 348\frac{\mathrm{km}}{\mathrm{s}}$ and $0.9 \leq w_i \leq 1.4$ and a $\mathrm{MpQ}(\mathrm{C}^{1+})$ histogram is created.

2. If necessary, background counts are substracted (cf. sec. 4.4.2).

3. The fit procedure explained in sec. 4.4.1 is performed.

4. By a numerical integration of the curve that was obtained for ion i the count rates of this ion species are determined. Note that for neon and magnesium also the isotopes are involved in the integration.

For every count rate determination this procedure is performed four times using bin widths of $0.25\frac{\mathrm{amu}}{e}$, $0.3\frac{\mathrm{amu}}{e}$, $0.35\frac{\mathrm{amu}}{e}$ and $0.4\frac{\mathrm{amu}}{e}$ in step 1) to compensate effects caused by the binning. For example, it can happen that due to the binning one MpQ bin contains more ToF channels than the other at the same EpQ-step that would result in a higher bin width.

To estimate the error of the count rate ratios, next to the standard deviation of the 4 results for each ion species, the confidence interval of the fitted parameters is used. For the peak height and the widths σ_l and σ_r the 1σ-confidence region is calculated for every result, from which a maximum and a minimum count rate can be calculated. The mean difference of these to the determined count rate serves as

another estimation of the count rate error and when considering count rate ratios, the propagation of errors has to be taken into account. The biggest error of the 4 results calculated with this approach is added quadratically to the statistical error to yield the total error of the count rate ratios. Therefore the estimated errors are quite large and likely to be overestimated. But as there can be quite large uncertainties in the count rates caused by the background or by overlapping peaks, a rather large error estimation is reasonable.

The results of this first approach are summarized in table 4.2 in the second column. The fits for the determination of the C^{1+} count rate, including background subtraction, are displayed in fig. 4.8. One can see on the one hand that the background substraction is necessary in the range of $0.9 \leq w_{C+} \leq 1.4$ and on the other hand that the peaks of Ne^{1+} and Mg^{1+} are still very small and thus neglegible. In fig. 4.9 the fit that was performed to determine the Si^{1+} count rate is shown. One can see that in this w-range, $0.9 \leq w_{Si+} \leq 1.4$, no background has to be subtracted and that the simultanous fit of all 7 ion peaks reproduces the data to a good extent and all peak shapes look reasonable.

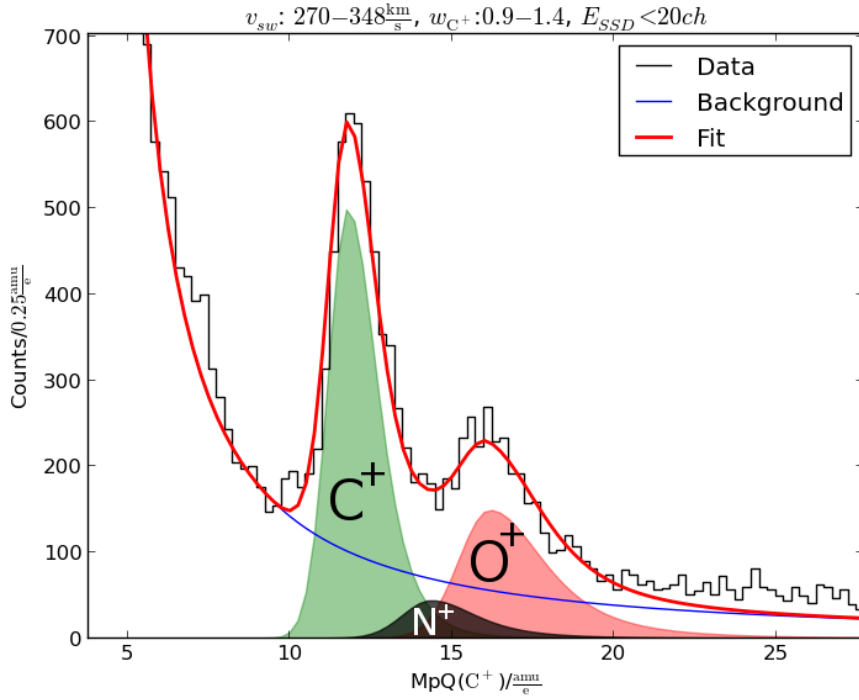

Figure 4.8: Fit in the corresponding MpQ-histogram for the determination of the C^{1+} count rate between $w = 0.9$ and $w = 1.4$ at solar wind speed up to $348\frac{km}{s}$. The blue line shows the subtracted background.
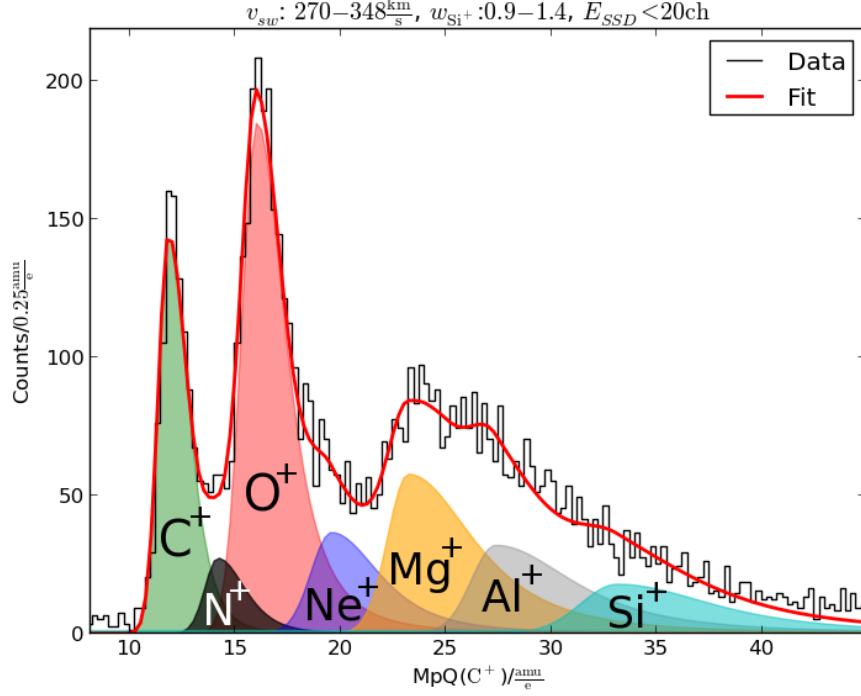
Figure 4.9: Fit in the corresponding MpQ-histogram for the determination of the Si^{1+} count rate between $w = 0.9$ and $w = 1.4$ at solar wind speed up to $348\frac{km}{s}$.

In contrast to Gloeckler et al. (2000) we observe Al^{1+} ions in the data. Although aluminium is quite rare as a solar wind element ($\frac{Al}{Mg} \approx 0.08$ (Bochsler, 2007)), it might be observable as PUI, because it has a very large photoionization cross-section. Furthermore, it is a very refractery element, which means that dust particles are likely to contain aluminium. Due to that neutral aluminium atoms could also originate from sputtering processes or dust-dust collisions. In the data one can see that it could close the gap between Mg^{1+} and Si^{1+} ions. As the peaks of the magnesium isotopes are very small, they are unlikely to close this gap. In fig. 4.10 the MpQ-histogram is shown, in which the Al^{1+} count rates have been determined. The red line displays the original fit including the Al^{1+} distribution. It has a reduced $\chi^2 = 0.98$ stating a high goodness of fit. The dashed blue line is a fit, where the Al^{1+} distribution was neglected. One can see that in the MpQ region of Al^{1+} the fit underestimates the data. Furthermore the reduced $\chi^2 = 1.19$ states a smaller goodness of fit, which supports the hypothesis of Al^{1+} ions to be present in the data. The gap between Mg^{1+} and Si^{1+} could also be closed by introducing a Fe^{2+} population, because these ions would peak at MpQ values similar to Al^{1+}. But as we expect these ions to leave a signature in the triple coincidence data (see
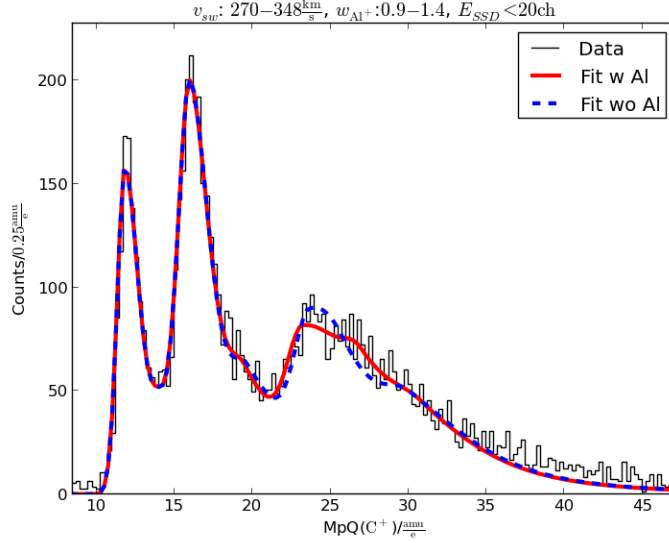
Figure 4.10: MpQ-histogram for the determination of the Al^{1+} count rate between $w = 0.9$ and $w = 1.4$ at solar wind speed up to $348\frac{km}{s}$. The red line shows the used fit, where the Al^{1+} has been taken into account. With this fit a goodness of fit of $\chi_{red} = 0.98$ is obtained. The dashed blue line shows a fit for which the Al^{1+} contribution was excluded with $\chi_{blue} = 1.19$ indicating a worse goodness.

also sec. 4.4.3), which is not the case, it is unlikely that the corresponding counts are caused by Fe^{2+} events.

As stated in chapter 1.3 it is assumed that the inner-source PUI velocity distributions evolve from the thermalization of PUI with the solar wind. Therefore the HPUI composition around $w = 1$ is investigated by determining the count rates of HPUIs in data filtered for w between 0.8 and 1.2. This means that the solar wind speed is limited to $v_{sw} < 407\frac{km}{s}$ due to the maximum speed of Si^{1+} that is covered by CTOF. In this w-range, especially when considering C^{1+} and N^{1+}, the background is quite big. The results from this procedure can also be found in table 4.2 in the third column.

The results can be compared to the solar wind elemental abundance ratios from von Steiger et al. (2000). The solar wind composition data was obtained during solar minimum at relatively low solar wind speeds and hence should be comparable to the considered time period and solar wind speeds used in the PUI analysis. There are production scenarios that propose that the inner-source PUIs originate from neutralized solar wind (Schwadron et al., 2000; Gloeckler et al., 2000; Wimmer-Schweingruber and Bochsler, 2003). If we assume that the elemental abundance ratio of neutralized solar wind ions equals the solar wind elemental abundance

59

Ion	$\frac{\text{Counts(Ion)}}{\text{Counts(O}^+)}$ (w:0.9-1.4)	$\frac{\text{Counts(Ion)}}{\text{Counts(O}^+)}$ (w:0.8-1.2)	Solar wind	Solar wind$\times\frac{\nu(\text{Ion})}{\nu(\text{O}^+)}$
C^{1+}	1.65 ± 0.23	1.76 ± 0.43	0.670 ± 0.040	1.70
N^{1+}	0.23 ± 0.15	0.12 ± 0.08	0.088 ± 0.022	0.09
O^{1+}	1	1	1	1
Ne^{1+}	0.30 ± 0.06	0.25 ± 0.05	0.104 ± 0.013	0.07
Mg^{1+}	0.65 ± 0.13	0.51 ± 0.09	0.143 ± 0.025	0.23
Al^{1+}	0.38 ± 0.06	0.26 ± 0.04	$0.0119 \pm 0.003^*$	5.89
Si^{1+}	0.25 ± 0.06	0.28 ± 0.06	0.132 ± 0.023	10.27

Table 4.2: Count rate ratios of HPUI measured in different w- and v_{sw}-ranges. In the second column the results from the measurement of v_{sw} up to $348\frac{\text{km}}{\text{s}}$ and w between 0.9 and 1.4 can be found. The third column corresponds to the values measured up to $407\frac{\text{km}}{\text{s}}$ and w between 0.8 and 1.2. The fourth column represents solar wind elemental composition values measured by von Steiger et al. (2000), except for *, which was taken from Bochsler (2007). In the last column these values were multiplied with the ratio of photoionization cross-sections ν as calculated following sec. 1.3.1.

ratios we can compute the HPUI composition that would be expected from such a source. This is done by just multiplying the solar wind elemental abundance ratios with the ratios of the photoionization cross-sections from sec. 1.3.1. These values can be found in the last column of table 4.2. If the inner-source is indeed located very close to the sun (cf. sec. 1.3) this approach would not be justified, because at regions with such a high EUV flux almost all produced neutrals would be rapidly ionized.

The HPUI composition values for C^{1+} and N^{1+} measured in the w-range from 0.8 to 1.2 match remarkably well with the weighted solar wind composition values. The small deviation of these values with those measured between $w = 0.9$ and $w = 1.4$ can be explained with an interstellar contribution to N^{1+} and O^{1+} which would be more pronounced at $0.9 \leq w \leq 1.4$ than at $0.8 \leq w \leq 1.2$. This is why more N^{1+} and O^{1+} compared to C^{1+} was observed between $w = 0.9$ and $w = 1.4$. In contrast to C^{1+} and N^{1+} the compositional values of the heavier PUI do not match with the values computed for the neutralized solar wind source in the fourth column. The deviation of the Ne^{1+} values can again be explained with an interstellar contribution that is very pronounced for Neon due to its high FIP (see also sec. 4.5.2). The overabundance of Mg^{1+} could be related to the underestimation of the Na^{1+} peak. Sodium has a very low FIP and could have a high ionization cross-section. Furthermore there is the possibility that counts of charged molecules that were not taken into account for the fitting of the data are superimposed on the Mg^{1+} peak. There is big uncertainty about the composition of the data at MpQ values larger than $22\frac{\text{amu}}{e}$, because the peaks become so wide that they can-

not be resolved from each other. Furthermore we have no information about the correctness of the MpQ conversion algorithm in this MpQ region and it could be that an imprecise conversion disturbs the analysis.

The compositional values for Al^{1+} and Si^{1+} are very low compared to the weighted solar wind values. The instrumental efficiency decreases strongly at larger MpQ values (see also sec. 2.3.4), which means that the real abundance ratios are probably larger than the measured values.

To gain better statistics the count rate ratios of C^{1+}, N^{1+} and O^{1+} are investigated independently from the other ions. This means that measurements up to a maximum solar wind speed of $v_{sw} = 460\frac{km}{s}$ can be used, because now the maximum speed $v_{max}(O^+) = 645\frac{km}{s}$ limits the usable solar wind speed range.

Ion	$\frac{\text{Counts(Ion)}}{\text{Counts(O}^+)}$
C^{1+}	1.25 ± 0.25
N^{1+}	0.21 ± 0.11

Table 4.3: Count rate ratios of C^{1+}/O^{1+} and C^{1+}/O^{1+} in the w-range between 0.9 and 1.4 in solar wind speeds up to $460\frac{km}{s}$.

In table 4.3 the results are displayed. It is obvious that the count rate ratio of C^{1+} to O^{1+} is significantly smaller than in the measurements before, while the N^{1+} to O^{1+} ratio seems to stay constant. As the same w-range was used in the measurements, the different solar wind speeds are probably the source for this. This is why the solar wind speed dependence of the C^{1+}, N^{1+} and O^{1+} count rate ratio is investigated in the following.

We expect that the C^{1+}/O^{1+} ratio decreases systematically with decreasing solar wind speed. This could then be the reason for the significantly lower C^{1+}/O^{1+} values in table 4.3. Therefore, the C^{1+}/O^{1+} and N^{1+}/O^{1+} abundance ratios have been determined from $300\frac{km}{s}$ to $537\frac{km}{s}$ in steps of $50\frac{km}{s}$ (except for the last one) in the w-range of $0.9 \leq w \leq 1.2$. The lower boundary, $w = 0.9$, was chosen to reduce background (cf. sec. 4.4.2). The upper boundary, $w = 1.2$, was chosen to enable the measurement at such high solar wind speeds.

The results are shown in table 4.4. One can see a clear trend of the C^{1+}/O^{1+} ratio to lower values at higher solar wind speeds, while the N^{1+}/O^{1+} ratio stays rather constant, which supports the thesis that the trend is a real effect and not caused by instrumental efficiencies.

To double check this, the C^{1+}/O^{1+} count rate ratio in the two time periods with different post-acceleration voltages are compared. The detection efficiency depends on the energy of the ions after post-acceleration (see sec. 2.3.4). Therefore the detection efficiency for an ion entering the sensor with a given energy should be larger with an increased post-acceleration voltage.

v_{sw}-range$/\frac{\text{km}}{\text{s}}$	$\frac{\text{Counts(C}^+)}{\text{Counts(O}^+)}$	$\frac{\text{Counts(N}^+)}{\text{Counts(O}^+)}$
$300 - 350$	1.61 ± 0.37	0.23 ± 0.14
$350 - 400$	1.51 ± 0.23	0.26 ± 0.14
$400 - 450$	1.23 ± 0.25	0.20 ± 0.09
$450 - 500$	1.11 ± 0.16	0.13 ± 0.08
$500 - 537$	1.02 ± 0.19	0.18 ± 0.10

Table 4.4: Count rate ratios of C^{1+}/O^{1+} and N^{1+}/O^{1+} in $0.9 \leq w \leq 1.2$ at varying solar wind speed ranges.

If the solar wind dependent C^{1+}/O^{1+} is caused by instrumental efficiencies, the efficiency of O^{1+} must increase strongly with solar wind speed and ion energy, respectively. However, the other condition is that the C^{1+} efficiency stays rather constant with increasing energy which could be due to the approaching of the efficiency limit (cf. fig. 2.2). To check if this is the case the following efficiency analysis was performed.

As the post-acceleration voltage was higher from DOY 150 to 230, a lower C^{1+}/O^{1+} ratio would be expected, if the efficiency of O^{1+} really increases in contrast to C^{1+}. At a speed of $v_{ion} = 350\frac{\text{km}}{\text{s}}$ a C^{1+} ion has a kinetic energy of $E_{kin} = 7.6\text{keV}$. The difference of the post-acceleration voltages is $\Delta U_p \approx 3.9\text{kV}$. This means that the post-acceleration energies of C^{1+} ions at $v_{ion} = 350\frac{\text{km}}{\text{s}}$ from DOY 150 to 230 correspond to C^{1+} ions at $v_{ion} \approx 430\frac{\text{km}}{\text{s}}$ ($E_{kin} = 11.5\text{keV}$) from DOY 82 to 145. This also means that they should have the same efficiencies when neglecting ion optical focussing effects. The count rate ratios in solar wind speeds from $330\frac{\text{km}}{\text{s}}$ to $350\frac{\text{km}}{\text{s}}$ for ions with $w = 1$ to $w = 1.2$ have been determined for the two time periods independently. The relatively high lower boundary for the w-range was chosen to minimize the effect of the background on the count rates that could be different in the two time periods. Additionally the ratio in the same w-range for solar wind speeds between $410\frac{\text{km}}{\text{s}}$ to $430\frac{\text{km}}{\text{s}}$ was determined. The results from this procedure are summarized in table 4.5. The two different values that were derived in $330\frac{\text{km}}{\text{s}} \leq v_{sw} \leq 350\frac{\text{km}}{\text{s}}$ suggest that the decrease of the C^{1+}/O^{1+} ratio at higher solar wind speeds might be related to different detection efficiencies of C^{1+} and O^{1+}. But in the second and third row the energy after post-acceleration of the measured ions was approximately the same. Nevertheless a lower value of C^{1+}/O^{1+} was measured at the different solar wind speed ranges. Moreover, a slightly lower C^{1+}/O^{1+} value was found in the last row, even though the detection efficiency for O^{1+} is increased due to the higher post-acceleration voltage. This proves that detection efficiencies cannot explain the observed correlation of solar wind speed and C^{1+}/O^{1+} ratio.

$v_{sw}/\frac{\text{km}}{\text{s}}$	U_p/kV	$E_{post}(\text{C}^+)$/keV	$\frac{\text{Counts(C}^+)}{\text{Counts(O}^+)}$
330-350	18.83	~ 26.4	2.35 ± 0.56
330-350	22.69	~ 30.3	1.74 ± 0.41
410-430	18.83	~ 30.3	1.35 ± 0.32
410-430	22.69	~ 34.2	1.40 ± 0.32

Table 4.5: Investigation of the detection efficiencies for C^{1+} and O^{1+}. The C^{1+}/O^{1+} ratio is shown for different solar wind speed ranges when a certain post-acceleration voltage was present. On can see that the solar wind speed dependent C^{1+}/O^{1+} cannot be explained by instrumental efficiencies.

4.5 w-spectra

PUIs are swept along with the solar wind, which means that their velocity depends on the present solar wind speed. Thus, PUI velocity spectra are always considered in terms of $w = \frac{v_{ion}}{v_{sw}}$, the ratio of ion and solar wind speed.
We again perform fits as explained above (sec. 4.4) to determine the count rates of ions in certain w-ranges. Now that the count rates of different ion speeds are compared, a phase-space correction is necessary. This is deduced in sec. 4.5.1. After that w-spectra for C^{1+}, O^{1+} and Ne^{1+} in different w-ranges are derived.

4.5.1 Velocity-space density

CTOF has a constant aperture angle and scans the velocity-space with the EpQ-filter that has a limited velocity-dependent bandwidth. This means that the velocity-space volume that is covered by the instrument depends on the current EpQ-step. If one wants to create PUI velocity spectra this has to be taken into account. When considering the HPUI composition, this correction is not necessary, because the same ion speeds are regarded for each species.
For EpQ-step j, the velocity-space volume can be calculated with the following formula:

$$V_{ps}^j = \int_{\Delta\frac{E_{kin}}{q_i}} \int_{\alpha} \int_{\beta} v^2 \sin(\alpha) \mathrm{d}v \mathrm{d}\alpha \mathrm{d}\beta \tag{4.5}$$

The opening angles of CTOF's aperture α and β are constant and hence the velocity-space volume only depends on the ion's velocity, v_i. Furthermore the bandwidth of the EpQ-filter is directly proportional to EpQ and thus it is directly

proportional to the ion's velocity. With this in mind one obtains:

$$V_{ps}^j \propto \int\limits_{\Delta \frac{E_{kin}}{q_i}} v_i^2 \mathrm{dv} \approx \mathrm{v_i^2} \Delta \mathrm{v_i} \propto \mathrm{v_i^3} \tag{4.6}$$

When considering multiple EpQ-steps, the covered phase-space volume is the sum of the individual phase-space volumes, because the proportionality constant is the same for every EpQ-step:

$$V_{ps} = \sum_j V_{ps}^j \propto \sum_j v_j^3 \tag{4.7}$$

The count rates in a velocity spectrum have to be corrected according to the velocity-space coverage of the used EpQ-steps.

4.5.2 Results

In the determination of the inner-source HPUI composition the count rates of different ions at constant w-ranges have been compared. Now we want to investigate the velocity distributions of C^{1+}, O^{1+} and Ne^{1+}. This means that we have to compare the count rates for the same ion species in different w-ranges to deduce a w-distribution.

When creating w-spectra it is crucial to check that the sensor covers all considered w's in the same way. This again means that the solar wind speed range that can be used is limited by the highest w for which count rates shall be obtained.

The procedure, how the w-spectra were created, must be split into two parts. First, w-spectra for $w > 1$ were obtained. In this w-range, the background substraction is rather simple and does not require a special treatment. After that w-spectra around $w = 1$ are created were the substraction of the background plays a bigger role.

When creating a w-spectrum for $w > 1$ the following steps were taken that are similar to the ones used in sec. 4.4.4:

1. The measured data is filtered for the corresponding w-range and solar wind speed. For the w-range always bin widths of $\Delta w = 0.05$ or $\Delta w = 0.1$ were used. For example, if one wants to determine the w-spectrum of C^{1+} from $w = 1$ to $w = 2$ with a bin width of $\Delta w = 0.1$, the data is first filtered for $1 \leq w_{C^+} \leq 1.1$. As the maximum speed of C^{1+} entering the CTOF sensor is $v_{max}(C^+) = 744 \frac{km}{s}$, the usable solar wind speed is limited to $v_{sw} < \frac{744 \frac{km}{s}}{2} = 372 \frac{km}{s}$.

2. From the data subset a $MpQ(C^{1+})$ histogram is created.

3. Background is substracted, if necessary.

4. The fit-procedure described in sec. 4.4.1 is applied to fit the peaks of the different ion species.

5. A numerical integration of the curve corresponding to the ion species of interest yields the count rate.

6. The w-spectrum is then integrated from the count rates in the w-bins used for the ion species under consideration.

Again MpQ bin widths of $0.25\frac{\text{amu}}{e}$, $0.3\frac{\text{amu}}{e}$, $0.35\frac{\text{amu}}{e}$ and $0.4\frac{\text{amu}}{e}$ are used in step 2) to avoid binning effects and to estimate the error.
In the w-spectrum the counts are always normalized to the highest phase-space corrected count rate. Thus, we always yield relative velocity-space densities.
The mean of the 4 normalized count rates is taken and the standard deviation serves as an error estimation, when neglecting the background error, which takes a bigger role at low velocities. An error derived from the confidence interval of the peak was neglected in this case, because now only count rates of one specific ion at different velocities are compared.
In the first approach, the w-range for C^{1+} up to $w = 2$ shall be covered, which limits the usable solar wind speed range to $v_{sw,max} = 372\frac{\text{km}}{\text{s}}$. This corresponds to maximum w values of $w = 1.7$ and $w = 1.55$ for O^{1+} and Ne^{1+}, respectively. As there are relatively many counts in this v_{sw}-range the bin width was set to $\Delta w = 0.05$. The corresponding w-spectra for C^{1+}, O^{1+} and Ne^{1+} are shown in the upper panel of fig. 4.11. We perform a second approach to achieve a bigger w-coverage. A similar w-spectrum has been derived with a limiting solar wind speed of $v_{sw,max} = 339\frac{\text{km}}{\text{s}}$. This sets the upper w-boundary for O^{1+} and Ne^{1+} to $w = 1.9$ and $w = 1.7$. As there are significantly less HPUI counts in this v_{sw}-range, the bin width was set to $\Delta w = 0.1$ and the fits were performed using Poisson statistics. The results for this are displayed in the lower panel of fig. 4.11.
One can see the clear difference between the C^{1+}, which is expected to be a pure inner-source PUI spectrum, and the O^{1+} and Ne^{1+} spectra, that can be mixtures of inner-source and interstellar spectra. The spectrum of C^{1+} shows an exponential decay towards higher w-values. The spectra of O^{1+} and Ne^{1+} show a similar behaviour at low values of w. At higher w values the spectra deviate from the C^{1+} spectrum by showing a tail. This tail is formed by interstellar PUIs that show a different velocity distribution than inner-source PUIs due to their different origin (cf. sec. 1.2). The Interstellar contribution of Ne^{1+} is more pronounced and about a factor 3 higher than for O^{1+} which can be explained by the very high FIP of neon. Due to the high FIP, neon atoms can penetrate deeply into the heliosphere.
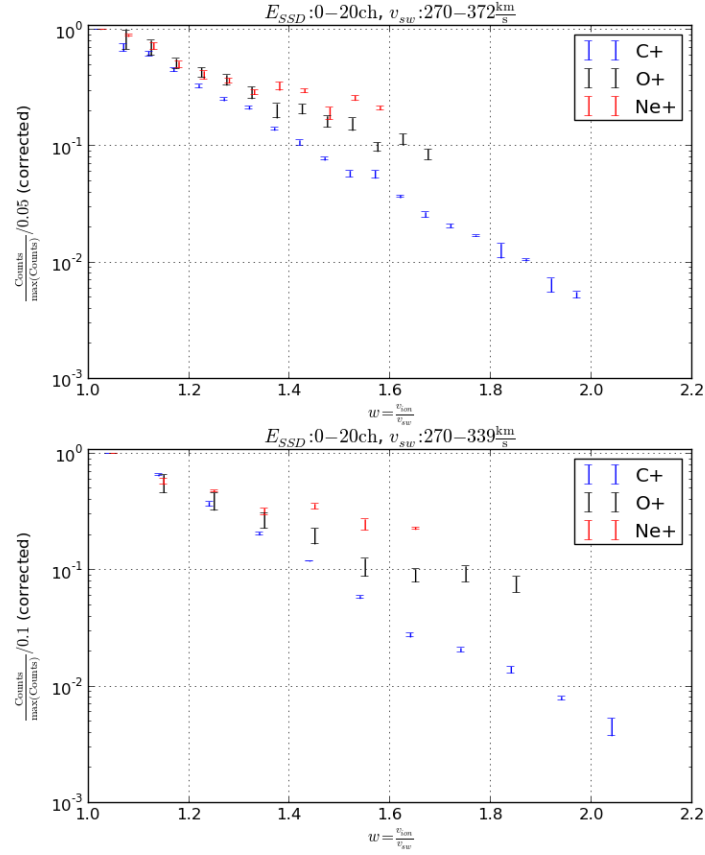
Figure 4.11: w-spectra for C^{1+}, O^{1+} and Ne^{1+} ion different v_{sw}-ranges. The count rates have been corrected for the phase-space coverage of the sensor. Upper panel: $270\frac{\text{km}}{\text{s}} \leq v_{sw} \leq 372\frac{\text{km}}{\text{s}}$ with a bin width of $\Delta w = 0.05$. Lower panel: $270\frac{\text{km}}{\text{s}} \leq v_{sw} \leq 339\frac{\text{km}}{\text{s}}$ with a bin width of $\Delta w = 0.1$.

This means that the probability for neon to reach 1AU is larger than the probability for oxygen. Thus, a more pronounced interstellar contribution can be observed for neon than for oxygen.

Consequently the inner-source Ne^{1+} abundance values from table 4.2 are overestimated, which might explain the deviation from the solar wind abundance values. Now the part around $w = 1$ of the spectra is investigated for C^{1+} and O^{1+}. Especially when considering the part with $w < 1$ the HPUI peaks are superimposed by background in the MpQ histograms, which is a big source of uncertainties and thus requires a special treatment. To reduce the influence of the background only

double coincidence data ($E_{SSD} = 0$) was considered, which only has a very small influence on the HPUI count rates, because at such low energies they can barely trigger a signal in the SSD. The count rates are derived in bins of $\Delta w = 0.05$.

The lowest bin edge, in which a peak for C^{1+} and O^{1+} can be fitted, is $w = 0.7$, where the peaks are barely visible by eye. At w values lower than this the background counts become too dominant. A value of $w_{C^+} = 0.7$ corresponds to $w_{He^+} \approx 1.2$, which means that in this speed range He^{1+} are not well suppressed and cause a big background.

When applying the procedure described above for C^{1+}, a 3-bin running average of the corresponding MpQ-histogram was calculated up to $w = 0.8$ to smooth the data. Furthermore only one Gauss-κ-function was fitted to the data up to $w_{C^+} = 0.85$. The peaks of N^{1+} and O^{1+} are still very small in this range, which means that the ratio of ion counts to background counts is too small to recognize a signature of these peaks. At higher w values the corresponding functions of these peaks were taken into account with the fit procedure described in sec. 4.4.1. When deriving the count rates of O^{1+}, only the peaks of C^{1+}, N^{1+} and O^{1+} were fitted up to $w_{O^+} = 0.9$. The peaks of the heavier ions are still very small at that low w-values. Furthermore the peaks get very broad at such low velocities which means that in the case of a large background these peaks cannot be distinguished from the underlying background counts. At higher values of w all ion distributions were used for fitting the peaks.

It is almost impossible to subtract the complex background precisely, because it contains of the superposition of many ToF tails from different ion species. Thus only estimations about the background shape can be made, which introduce large errors in the count rates that shall be derived. To estimate the error, always a minimal, a maximal and an "optimal" curve is fitted to the background and the fit of the peaks is performed with each background substraction. An example of these three curves is shown in fig. 4.12. It has to be mentioned that this procedure and especially the fit of the "optimal" curve is subjective to a great extent. But this is the only way to get a reasonable estimate of the count rate error without having a sophisticated model of the background. As it can be expected that the error caused by the background is far bigger than the error caused by binning or fit effects, the count rates are only derived in MpQ-histograms with a bin width of $0.25 \frac{amu}{e}$.

In fig. 4.13 overall 4 results from this procedure are shown. First, the solar wind speed range from $330 \frac{km}{s}$ to $370 \frac{km}{s}$ was chosen, because in this interval most of the double coincidence counts were measured. Furthermore the speed interval from $400 \frac{km}{s}$ to $500 \frac{km}{s}$ was investigated to see if any differences in the w-distribution in faster solar wind streams can be found. The red curve is a total average from all data points in the figure that was illustrated to guide the eye.
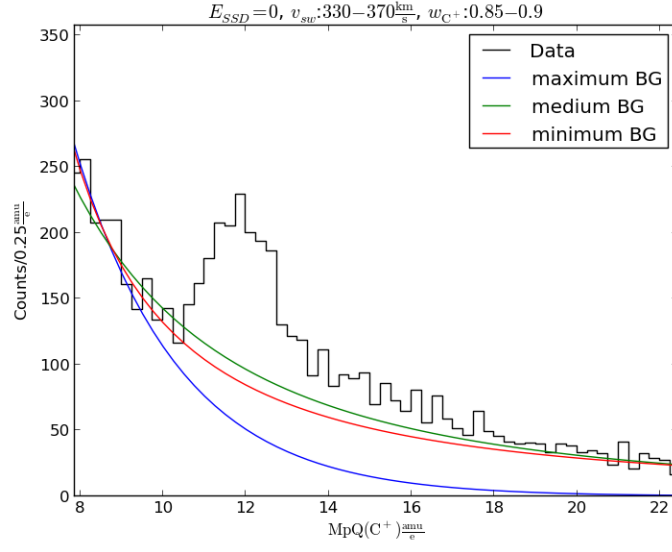
Figure 4.12: MpQ-histogram of counts with $w : 0.85 - 0.9$, $v_{sw} : 330 - 370\frac{\text{km}}{\text{s}}$ and $E_{SSD} = 0$. Three curves estimating the background have been fitted to derive a value for the count rate error.

Even with errors that big, one can see that the spectra peak at $w \approx 0.8$ rather than at $w = 1$. Unfortuntely no other reliable statements about the spectra can be made and no differences between the spectra can be seen due to the big errors.
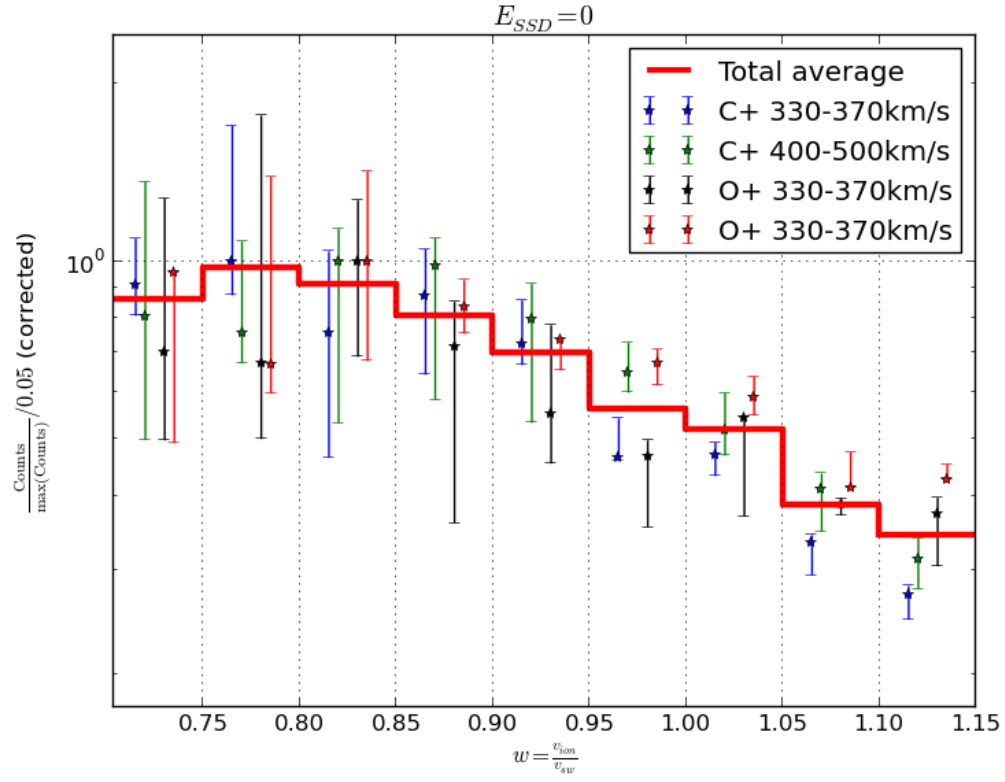
Figure 4.13: w-spectra from $w = 0.7$ to $w = 1.15$ for C^{1+} and O^{1+} at different solar wind speeds. For a better display of the data, the data points are not in the middle of the corresponding bin.

Chapter 5

Summary and conclusion

5.1 Conclusions

5.1.1 Inner-source HPUI composition

Overall it was found that for C^{1+}, N^{1+}, O^{1+} and Ne^{1+} the inner-source HPUI composition matches remarkably well the solar wind elemental composition when taking ionization cross-setions and the underlying interstellar contribution (for the last three ions) into account. The deviation of the Mg^{1+} ions could be due to further ion species or charged molecules that are superimposed on the Mg^{1+} counts. It is also possible that we underestimated the contribution of Na^{1+} to the MpQ-spectrum. It is just taken into account in the fit as a constant peak that is not optimized.

The ratios of Al^{1+} and Si^{1+} to O^{1+} are larger than the solar wind elemental abundance ratios. This could be due to their larger photoionization cross-sections. But from that point of view one would expect far more Al^{1+} and Si^{1+} counts than observed. One has to keep in mind that the detection efficiency rapidly decreases for heavier ions (cf. fig. 2.2), which means that the real Al^{1+}/O^{1+} and Si^{1+}/O^{1+} ratios in the solar wind are likely to be larger. Another effect that could play a role is that some of the aluminium and silicon PUIs could get doubly ionized. Then they would be measured in the MpQ range of nitrogen and would falsely contribute to this peak. Moreover, related to the low FIP of these elements, the ion production of Al^{1+} and Si^{1+} could be limited to the production of neutrals. For example, there is a neutral component of oxygen and aluminium in the solar wind. Let x_{Al} be the number of neutral aluminium atoms and x_O be the number of neutral oxygen atoms with an abundance ratio of $\frac{x_{Al}}{x_O} \approx 0.012$. Let's assume that due to photoionization about 10% of the oxygen ions get ionized. Because of its high photoionization cross-section about 500 times more aluminium atoms would get ionized than oxygen atoms (see table 1.2). But there is only a limited number

x_{Al} of aluminium atoms and a maximum of 100% can get ionized. Then the ratio of Al^{1+}/O^{1+} would yield: $\frac{x_{Al}}{0.1 x_O} \approx 0.12$. Of course, this example is oversimplified. But it makes clear that the production rate of HPUIs like Al^{1+} or Si^{1+} could be limited by the presence of neutrals.

The derived values from our analysis are generally consistent with those determined by Gloeckler et al. (2000), which can be found in table 1.1, within the estimated uncertainties. One exception is the abundance ratio of N^{1+}/O^{1+} determined by Gloeckler et al. (2000) that deviates by a factor of 2 from our findings. However, the ratio that was determined by our data analysis matches the solar wind elemental composition ratio to a better extent. In this case one can neglect the photoionization cross-sections, because they are expected to be approximately equal for nitrogen and oxygen (see table 1.2). Another exception is that we also considered Al^{1+} ions in our analysis that were neglected by Gloeckler et al. (2000).

5.1.2 Solar wind speed dependend C^{1+}/O^{1+} ratio

In sec. 4.4.4 the inner-source C^{1+}/O^{1+} ratio was investigated at different solar wind speed ranges. The determined ratios that are shown in table 4.4 show that the C^{1+}/O^{1+} ratio tends to lower values at higher the solar wind speeds. With the help of the determined values shown in table 4.5 it could be proved that this tendency does not originate from instrumental efficiencies.

Thus at higher solar wind speeds either the abundance of C^{1+} ions decreases or the abundance of O^{1+} ions increases in the considered w-range. As we are only considering count rate ratios we cannot say clearly which is the case. Nevertheless conjectures about the implications of this for the proposed inner-source PUI production scenarios (sec. 1.3) can be made. In the solar wind recycling scenario sputtering of grain material and the implanted ions may play a role and at higher solar wind speeds the sputtering rate should increase. Interplanetary dust grains are supposed to contain far more carbon than oxygen and hence one would rather expect that more C^{1+} ions are produced from this scenario at higher solar wind speeds. But the observations in table 4.4 could not only be caused by different abundances. Also a shift in the velocity distribution of these ions could be possible, because only a small w-range was considered.

One interesting thing to find out would be if the solar wind speed dependent C^{1+}/O^{1+} ratio is also correlated to the general C/O elemental abundance ratio in the solar wind, because it is known that there are speed dependent composition variations in the solar wind, for example the Mg/O ratio (cf. von Steiger et al. (1995)). This would provide another hint for the validity of the solar wind neutralization scenario. In general, this observation is another characteristic for the inner-source PUIs that must now be investigated in the context of the proposed production scenarios.

5.1.3 w-spectra

The w-spectra with $w > 1$ are consistent with those derived by Gloeckler and Geiss (1998) with ULYSSES/SWICS. We could show that the interstellar contribution of neon is more pronounced than for oxygen. This was used to explain the deviation of the Ne^{1+}/O^{1+} ratio from the solar wind elemental abundance ratio and the elemental abundance ratio multiplied with the ratio of photoionization cross-sections, respectively.

The w-spectra that were derived around $w = 1$ suffer from large errors that are caused by background counts. Nevertheless it was shown that the w-spectra of C^{1+} and O^{1+} peak at $w \approx 0.8$. This was also already observed with ULYSSES/SWICS by Gloeckler and Geiss (1998).

One possibility to explain the peak at $w \approx 0.8$ is related to the production mechanism of inner-source HPUIs. According to Wimmer-Schweingruber and Bochsler (2003) PUI might be produced by solar wind ions passing through very thin dust grains (sec. 1.3). When passing these grains the ions loose a part, but not all of their energy, which means that they already have a certain velocity when being injected into the solar wind as PUI. In fig. 5.1 the results from TRIM simulations illustrating this are shown. The passage of carbon ions at $w = 1$ through 100Å of carbon was simulated at different solar wind speeds. From the transmitted energy, the w of the particles after exiting the foil was calculated and histogramed. One can see that the distributions peak at $w \approx 0.8 - 0.9$. Therefore the w-spectrum that is observed in fig. 4.13, might be the consequence of freshly injected PUIs having a slower velocity than the solar wind due to their interaction with tiny dust grains. This theory somehow resembles the findings of Drews et al. (2013) that the interstellar PUI velocity spectrum shows a beam structure caused by freshly injected PUI of interstellar origin.

5.2 Summary

In this Master thesis HPUIs were studied using data obtained with the CTOF sensor of the CELIAS experiment onboard the SOHO spacecraft. First, a MpQ-conversion function that is necessary to identify HPUIs was derived successfully from long-term data measured in-flight. Additionally a model for the peak-shapes of the considered ions in MpQ-spectra was developed using TRIM simulations. Both, the MpQ-conversion and the peak shape prediction, were used to investigate the composition and velocity spectra of inner-source HPUIs.

It was found that the abundances of inner-source C^{1+}, N^{1+}, O^{1+}, and Ne^{1+} closely match the solar wind abundances when taking ionization cross-sections into ac-
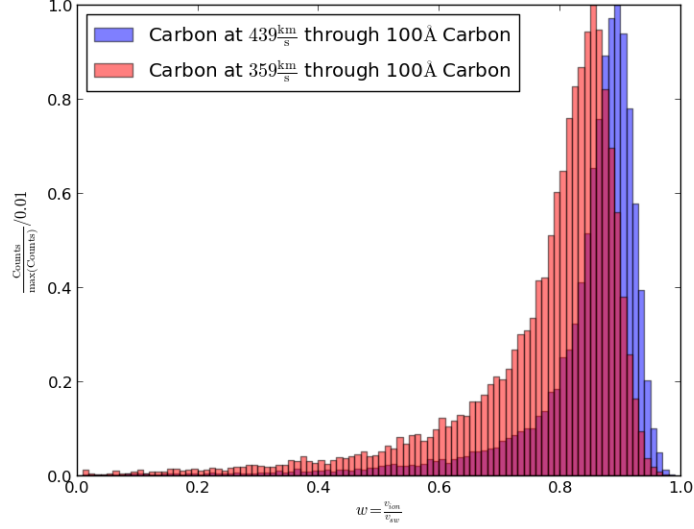
Figure 5.1: Histogram of the w values for Carbon ions at $w = 1$ passing through 100Å of Carbon at different solar wind speeds simulated with TRIM.

count. Furthermore the existence of Al^{1+} ions in the data was proposed. The observed abundances of Mg^{1+}, Al^{1+} and Si^{1+} do not resemble the weighted solar wind values. Multiple possibilities that could lead to such a deviation were discussed. The findings will be summarized in a paper that will be submitted for publication.

Furthermore the w-spectra revealed that the interstellar PUI component is more pronounced for Ne^{1+} than for O^{1+}, which explains the high count rates of Ne^{1+} in the inner-source PUI composition estimation, and that the inner-source w-distributions probably peak between $w = 0.8$ and $w = 0.9$. Both findings are neither new nor unique, but consistent with previous work of Gloeckler et al. (2000), for example.

5.3 Outlook

The MpQ-conversion used in this thesis could be improved by considering the angular scattering of the ions when passing the carbon foil in the in-flight calibration. Then a more accurate peak shape prediction might be possible, which would be an advantage for the whole data analysis, that has been performed. With a more precise knowledge of the position and shape of the peaks in a MpQ-histogram a better resolution of the Mg^{1+}, Al^{1+}, Si^{1+} and maybe further ion species might be possible. Furthermore this could help to develop a more sophisticated model for

the background which would be an advantage in the analysis of w-spectra.

Unfortunately the SOHO spacecraft does not carry a magnetometer, which means that we have no information about the orientation of the present magnetic field. This would have been an advantage for PUI studies, especially when investigating velocity spectra, because the initial velocity of a PUI is dependent on the magnetic field configuration. But from the differential streaming of heavy ions in the solar wind (see also Janitzek (2014)) it may be able to estimate the local magnetic field orientation.

A very prominent PUI that has not been considered in this analysis is He^{1+}. It would be quite easy to apply the analysis technique to this ion species to derive velocity spectra and to deduce inner-source He^{1+} abundance values. Moreover, CTOF's large geometric factor could be used to investigate HPUIs on the basis of short term data. This is one of the main advantages of this instrument compared to ULYSSES/SWICS, for example. Thus, time dependent or further solar wind speed dependent HPUI composition variations could be investigated.

A virtual detector similar to the one used in Drews et al. (2013) for STEREO/PLASTIC should be implemented for CTOF to investigate how certain input velocity distributions would manifest themselves as count rate spectra in CTOF. Furthermore simulations should be run to test the implications of a local inner-source PUI production by the interaction of solar wind ions with tiny dust grains.

But one has to always remember that CTOF's data is limited due to its early breakdown on DOY 230, 1996, and one needs to strike a balance between the effort put into the analysis and the possible science output.

Appendix A

Curve Fitting

When given a set of n data points with $x = (x_1, x_2, .., x_n)$ and $y = (y_1, y_2, .., y_n)$, superimposed by random noise, and a mathematical function $y = f(x, \vec{a})$ is assumed to be the relation between the data points, the parameters of the function, $\vec{a}$, leading to the best fit of the function to the data can be calculated.

The main idea of the procedure is to find a **M**aximum **L**ikelihood **E**stimate (MLE) of the parameters, which means that the probability, p, that the data points derive from the estimated parameters is maximized. The deviation of the data points from the model is considered by two types of statistics in this thesis: Gaussian- and Poisson-statistics. For both statistics the procedure of finding the parameters for a best fit is described in the following. Further information on curve fitting and a more detailed explanation of the methods used can be found in Press (2007).

A.1   Gaussian statistics

We assume that the noise that is superimposed over our data points is distributed by a Gaussian. This means that the probability $p(x_i, y_i, \vec{a})$ that we measure the value y_i at the position x_i with a given set of parameters $\vec{a}$ is

$$p_i^G(x_i, y_i, \vec{a}) = \frac{1}{\sigma_i \sqrt{2\pi}} \exp\left(-\frac{(y_i - f(x_i, \vec{a}))^2}{2\sigma_i^2}\right). \qquad (A.1)$$

The standard error of each measurement is denoted σ_i. As we usually deal with count rates in this thesis the standard error of one data point can be assumed to be $\sigma_i = \sqrt{y_i}$ in this case.

The total probability that the set of n data points derive from the given function and parameters is then the product of each probability. This probability must be

maximized to find the optimal set of parameters for a best fit as stated above.

$$p_{tot}^G(x, y, \vec{a}) = \prod_{i=1}^{n} p_i^G(x_i, y_i, \vec{a}) \tag{A.2}$$

It is useful to apply the natural logarithm to this equation to convert the product into a sum.

$$\ln\left(p_{tot}^G(x, y, \vec{a})\right) = \ln\left(\prod_{i=1}^{n} p_i^G(x_i, y_i, \vec{a})\right) = \sum_{i=1}^{n} \ln\left(p_i(x_i, y_i, \vec{a})\right) \tag{A.3}$$

$$= \sum_{i=1}^{n} \left(\ln\left(\frac{1}{\sigma_i\sqrt{2\pi}}\right) - \frac{(y_i - f(x_i, \vec{a}))^2}{2\sigma_i^2}\right) \tag{A.4}$$

The natural logharitm is a steady function. Thus it makes no difference either to maximize p_{tot}^G or $\ln(p_{tot}^G)$. For computational reasons it is more convenient to consider a minimization than a maximization problem. Therefore, $-\ln(p_{tot}^G)$ is minimized instead of maximizing $\ln(p_{tot}^G)$. The first term of eqn. A.4 does not depend on $\vec{a}$ and is thus constant and neglegible. Furthermore, the second term can be multiplied by 2 and we are left with the final minimization problem:

$$-\ln(\tilde{p}_{tot}^G(x, y, \vec{a})) = \sum_{i=1}^{n} \frac{(y_i - f(x_i, \vec{a}))^2}{\sigma_i^2} \tag{A.5}$$

The numerator of the fraction on the right hand side of eqn. A.5 is the deviation of data and model squared and weighted with the denominator which is the squared standard error of the data. Therefore this method is commonly known as least-squares fitting. The minimzation of eqn. A.5 itself is performed by the very robust and well-established Levenberg-Marquardt algorithm (Press, 2007). A problem with this algorithm is that it only provides a local minimum, which is not necessarily a global minimum. But by a sophisticated choice of starting parameters, parameter boundaries and other tricks a global or at least a physically reasonable minimum can be achieved.

The goodness of fit can be evaluated by calculating the reduced χ^2:

$$\chi^2 = \frac{1}{n-m} \sum_{i=1}^{n} \frac{(y_i - f(x_i, \vec{a}))^2}{\sigma_i^2} \tag{A.6}$$

The difference of the number of data points n and the number of parameters m gives the degrees of freedom. A perfect fit of model and data would yield a reduced $\chi^2 = 1$. A reduced $\chi^2 >> 1$ states a poor goodness of fit and a reduced $\chi^2 < 1$ can be explained with an overestimation of errors.

A.2   Poisson statistics

For counting experiments the underlying statistics is not Gaussian but Poissonian. For a sufficient number of counts this difference is irrelevant, but for small count numbers the difference can be important.

The derivation of the minimization problem of the MLE with Poisson statistics is basically the same as with Gaussian statistics. The fundamental difference is to replace the Gaussian distribution by a Poisson distribution in eqn. A.1. Now we assume that the variation of the data from the model follows a Poisson distribution, which means that we can describe the probability to measure the value y_i that depends on x_i by

$$p_i^P(x_i, y_i, \vec{a}) = \frac{\lambda^k}{k!} e^{-\lambda} = \frac{f(x_i, \vec{a})^{y_i}}{y_i!} e^{-f(x_i, \vec{a})} \tag{A.7}$$

with $\lambda = f(x_i, \vec{a})$, which is both expectation value and variance, the integer $k = y_i$ and of course a given model function $f(x_i, \vec{a})$ with a set of parameters $\vec{a}$. The next steps are analogous to the steps taken in section A.1. Again the total probability is built from the product of the single probabilities, the natural logarithm is applied and the maximization problem is converted into a minimization problem. The result is

$$-\ln(p_{tot}^P(x, y, \vec{a})) = \sum_{i=1}^{n} \left(f(x_i, y_i, \vec{a}) - \ln\left(\frac{f(x_i, y_i, \vec{a})^{y_i}}{y_i!} \right) \right) \tag{A.8}$$

$$= \sum_{i=1}^{n} \left(f(x_i, y_i, \vec{a}) - y_i \ln(f(x_i, y_i, \vec{a})) + \ln(y_i!) \right) \tag{A.9}$$

As $\ln(y_i!)$ is constant and known, it is of no importance for the minimization and can be neglected. Finally the minimzation problem reads

$$-\ln(\tilde{p}_{tot}^P(x, y, \vec{a})) = \sum_{i=1}^{n} \left(f(x_i, y_i, \vec{a}) - y_i \ln(f(x_i, y_i, \vec{a})) \right). \tag{A.10}$$

For this minimization different algorithms can be applied. In this thesis the Nelder-Mead method was chosen, because it provides a more global search of the minimum and copes with the optimization of many parameters at once.

A.3   Implementation

The fits in this thesis were performed in `Python` by using the `scipy.optimize` package and the module `lmfit`. The `scipy.optimize`[1] package contains multiple

---

[1]http://docs.scipy.org/doc/scipy/reference/optimize.html

minimization and root-finding routines written either in `C`, `Fortran` or `Python` code. Especially the Levenberg-Marquardt algorithm (`optimize.leastsq`) and the Nelder-Mead method (`optimize.fmin`), that are used in this thesis, are implemented in this package.

The `lmfit`[2] module itself is an interface for `scipy.optimize`, because it resorts on the methods just named in an object-oriented way. One of the main advantages of this module is the object-oriented parameter handling that makes it possible to easily set constraints and dependencies for the variables.

Another feature of this module is the capability of calculating confidence intervals following the so-called F-test (Press, 2007). We used it in this thesis for the estimation of errors.

---

[2]http://lmfit.github.io/lmfit-py/

Appendix B

List of abbreviations

List of every abbreviation used in this report in alphabetical order except for mission or instrument names:

ADC	Analog-digital converter
DPU	Data processing unit
DOY	Day of year
EpQ	Enery per charge
EUV	Extreme ultra-violet
FIP	First ionization potential
HPUI	Heavy pickup ion
LISM	Local interstellar medium
MCP	Microchannel-plate
MpQ	Mass per charge
PHA	Pulse height analysis
PM	Proton monitor
PUI	Pickup ion
SSD	Solid-state Detector
SW	Solar wind
ToF	Time-of-flight

Bibliography

M.R. Aellig. *Freeze-in Temperatures and Relative Abundances of Iron Ions in the Solar Wind Measured With SOHO/CELIAS/CTOF*. PhD thesis, Universität Bern, 1998.

F Allegrini, NA Schwadron, DJ McComas, G Gloeckler, and J Geiss. Stability of the inner source pickup ions over the solar cycle. *Journal of Geophysical Research: Space Physics (1978–2012)*, 110(A5), 2005.

Markus J Aschwanden. *Physics of the Solar Corona: An Introduction with Problems and Solutions*. Springer, 2005.

L Berger, C Drews, A Taut, and RF Wimmer-Schweingruber. Heavy pickup ion w-spectra at 1 au with soho/celias/ctof. In *AIP Conference Proceedings*, volume 1539, page 386, 2013.

Peter Bochsler. Minor ions in the solar wind. *The Astronomy and Astrophysics Review*, 14(1):1–40, 2007.

M Bzowski and M Królikowska. Are the sungrazing comets the inner source of pickup ions and energetic neutral atoms? *arXiv preprint astro-ph/0405148*, 2004.

Christian Drews, Lars Berger, Robert F Wimmer-Schweingruber, Peter Bochsler, Antoinette B Galvin, Berndt Klecker, and Eberhard Möbius. Inflow direction of interstellar neutrals deduced from pickup ion measurements at 1 au. *Journal of Geophysical Research: Space Physics (1978–2012)*, 117(A9), 2012.

Christian Drews, Lars Berger, Robert F Wimmer-Schweingruber, and Antoinette B Galvin. Interstellar he+ ring-beam distributions: Observations and implications. *Geophysical Research Letters*, 2013.

Bernhard Fleck. The soho mission. *Coronal Magnetic Energy Releases*, pages 233–244, 1995.

Priscilla C Frisch, Seth Redfield, and Jonathan D Slavin. The interstellar medium surrounding the sun. *Annual Review of Astronomy and Astrophysics*, 49:237–279, 2011.

J Geiss, G Gloeckler, LA Fisk, and R von Steiger. C+ pickup ions in the heliosphere and their origin. *Journal of Geophysical Research: Space Physics (1978–2012)*, 100(A12):23373–23377, 1995.

J Geiss, G Gloeckler, and R Von Steiger. Origin of c+ ions in the heliosphere. In *The Heliosphere in the Local Interstellar Medium*, pages 43–52. Springer, 1996.

G Gloeckler, LA Fisk, J Geiss, NA Schwadron, and TH Zurbuchen. Elemental composition of the inner source pickup ions. *Journal of Geophysical Research: Space Physics (1978–2012)*, 105(A4):7459–7463, 2000.

George Gloeckler and Johannes Geiss. Interstellar and inner source pickup ions observed with swics on ulysses. *Space Science Reviews*, 86(1-4):127–159, 1998.

H Grünwaldt, M Neugebauer, M Hilchenbach, P Bochsler, D Hovestadt, A Bürgi, FM Ipavich, K-U Reiche, WI Axford, H Balsiger, et al. Venus tail ray observation near earth. *Geophysical research letters*, 24(10):1163–1166, 1997.

S. Hefti. *Solar wind freeze-in temperatures and fluxes measured with SOHO/CELIAS/CTOF and calibration of the CELIAS sensors*. PhD thesis, Universität Bern, 1997.

Arnold F Holleman, Egon Wiberg, and Nils Wiberg. *Lehrbuch der anorganischen Chemie*. Walter de Gruyter, 1995.

D Hovestadt, M Hilchenbach, A Bürgi, B Klecker, P Laeverenz, M Scholer, H Grünwaldt, WI Axford, S Livi, E Marsch, et al. Celias-charge, element and isotope analysis system for soho. *Solar Physics*, 162(1):441–481, 1995.

Nils Janitzek. High time resolution measurements with soho/celias/ctof. Master's thesis, CAU Kiel, 2014.

M. Köten. *An Improved Efficiency Model for ACE-SWICS Determination of the Carbon Isotopic Ratio 13C, 12C in the Solar Wind from ACE-SWICS Mesasurements*. PhD thesis, CAU Kiel, 2009.

J Lindhard and M Scharff. Energy dissipation by ions in the kev region. *Physical Review*, 124(1):128, 1961.

Ingrid Mann and Andrzej Czechowski. Dust destruction and ion formation in the inner solar system. *The Astrophysical Journal Letters*, 621(1):L73, 2005.

E Möbius, D Hovestadt, B Klecker, M Scholer, and G Gloeckler. Direct observation of he (+) pick-up ions of interstellar origin in the solar wind. *Nature*, 318:426–429, 1985.

M Oka, T Terasawa, H Noda, Y Saito, and T Mukai. 'torus' distribution of interstellar helium pickup ions: Direct observation. *Geophysical research letters*, 29(12):1612, 2002.

William H Press. *Numerical recipes 3rd edition: The art of scientific computing*. Cambridge university press, 2007.

Lukas Saul, Eberhard Möbius, Philip Isenberg, and Peter Bochsler. On pitch-angle scattering rates of interstellar pickup ions as determined by in situ measurement of velocity distributions. *The Astrophysical Journal*, 655(1):672, 2007.

Lukas Saul, Peter Wurz, and Reinald Kallenbach. A measurement of the adiabatic cooling index for interstellar helium pickup ions in the inner heliosphere. *The Astrophysical Journal*, 703(1):325, 2009.

NA Schwadron, J Geiss, LA Fisk, G Gloeckler, Th H Zurbuchen, and R von Steiger. Inner source distributions: Theoretical interpretation, implications, and evidence for inner source protons. *Journal of Geophysical Research: Space Physics (1978–2012)*, 105(A4):7465–7472, 2000.

Bruce T Tsurutani and Gurbax S Lakhina. Some basic concepts of wave-particle interactions in collisionless plasmas. *Reviews of Geophysics*, 35(4):491–501, 1997.

VM Vasyliunas and GL Siscoe. On the flux and the energy spectrum of interstellar ions in the solar system. *Journal of Geophysical Research*, 81(7):1247–1252, 1976.

DA Verner, GJ Ferland, KT Korista, and DG Yakovlev. Atomic data for astrophysics. ii. new analytic fits for photoionization cross sections of atoms and ions. *arXiv preprint astro-ph/9601009*, 1996.

R von Steiger, RF Wimmer Schweingruber, J Geiss, and G Gloeckler. Abundance variations in the solar wind. *Advances in Space Research*, 15(7):3–12, 1995.

R von Steiger, N Schwadron, LA Fisk, J Geiss, G Gloeckler, S Hefti, B Wilken, RF Wimmer-Schweingruber, and TH Zurbuchen. Composition of quasistationary solar wind flows from ulysses/solar wind ion composition spectrometer. *Journal of Geophysical Research*, 105(A12):27217–27238, 2000.

Roger C Wiens, Peter Bochsler, Donald S Burnett, and Robert F Wimmer-Schweingruber. Solar and solar wind isotopic compositions. *Earth and Planetary Science Letters*, 226(3):549–565, 2004.

Robert F Wimmer-Schweingruber and Peter Bochsler. On the origin of inner-source pickup ions. *Geophysical research letters*, 30(2), 2003.

Robert F Wimmer-Schweingruber, Peter Bochsler, Olivier Kern, George Gloeckler, and Douglas C Hamilton. First determination of the silicon isotopic composition of the solar wind: Wind/mass results. *Journal of Geophysical Research: Space Physics (1978–2012)*, 103(A9):20621–20630, 1998.

James F Ziegler, MD Ziegler, and JP Biersack. Srim–the stopping and range of ions in matter (2010). *Nuclear Instruments and Methods in Physics Research Section B: Beam Interactions with Materials and Atoms*, 268(11):1818–1823, 2010.

Appendix C

Formalities

Erklärung gemäß Paragraph 9 Abs. 7 der Prüfungsverfahrensordnung der Christian-Albrechts-Universität zu Kiel für Studierende der Bachelor- und Master-Studiengänge

Hiermit erkläre ich, dass ich die Masterarbeit selbstständig verfasst und keine anderen als die angegebenen Quellen und Hilfsmittel benutzt habe und die Arbeit in keinem anderen Prüfungsverfahren eingereicht habe.

_____   _____
Ort, Datum   Unterschrift

Danksagung

Zunächst möchte ich Prof. Dr. Wimmer-Schweingruber für die Vergabe dieser Arbeit und die Möglichkeit in diesem faszinierenden Forschungsgebiet zu arbeiten danken.

Des Weiteren danke ich Dr. Lars Berger für die exzellente Betreuung und, zusammen mit Dr. Christian Drews, die Bereitstellung von `dbData`, ohne das diese Arbeit nicht möglich gewesen wäre.

Natürlich gilt mein Dank auch der gesamten Solar Wind meeting Crew, die mit guten Diskussionen die Arbeit immer wieder vorangebracht hat. Daraus hervorzuheben ist Nils Janitzek, dessen kritisches Hinterfragen oft neue Erkenntnisse brachte.

Für die großartige Zeit, während des Studium möchte ich Robert Elftmann, Sebastian Groth, Steven Huth und Frederik Woltering (und nicht zu vergessen Albert) danken, die immer dafür gesorgt haben, dass ich auf dem Boden der Tatsachen geblieben bin.

Für die Finanzierung meiner letzten beiden Semester und des Segelkurses möchte ich Peter Stier danken, der mir dies mit einem Deutschlandstipendium ermöglicht hat. Außerdem möchte ich Frau Müller aus dem Prüfungsamt danken.

Ein ganz besonderer Dank geht an meine Freundin Sonja, die mir nicht nur mit einigen Grafiken geholfen hat, sondern auch allgemein dafür sorgt, dass ich bei Verstand bleibe. Ebenso möchte ich meiner Familie danken, die mir dieses Studium überhaupt erst ermöglicht hat.